https://doi.org/10.5194/egusphere-2025-2473
Preprint. Discussion started: 12 June 2025

The ICON-based Earth System Model for Climate Predictions and Projections (ICON XPP v1.0)

Wolfgang A. Müller[1], Stephan Lorenz[1], Trang V. Pham[2], Andrea Schneidereit[2], Renate Brokopf[1], Victor Brovkin[1,6], Nils Brüggemann[1], Fatemeh Chegini[1], Dietmar Dommenget[3], Kristina Fröhlich[2], Barbara Früh[2], Veronika Gayler[1], Helmuth Haak[1], Stefan Hagemann[4], Moritz Hanke[5], Tatiana Ilyina[6], Johann Jungclaus[1], Martin Köhler[2], Peter Korn[1], Luis Kornblueh[1], Clarissa A. Kroll[7], Julian Krüger[1], Karel Castro-Morales[2], Ulrike Niemeier[1], Holger Pohlmann[1], Iuliia Polkova[2], Roland Potthast[2], Thomas Riddick[1], Manuel Schlund[8], Tobias Stacke[1], Roland Wirth[2], Dakuan Yu[1], and Jochem Marotzke[1]

[1] *Max-Planck Institute for Meteorology, Hamburg, Germany*

[2] *Deutscher Wetterdienst, Offenbach am Main, Germany*

[3] *ARC Centre of Excellence for Climate Extremes, Monash University, Australia*

[4] *Institute of Coastal Systems, Helmholtz-Zentrum Hereon, Geesthacht, Germany*

[5] *Deutsches Klimarechenzentrum, Hamburg, Germany*

[6] *University of Hamburg, Hamburg, Germany*

[7] *ETH Zürich, Zürich, Switzerland*

[8]*Deutsches Zentrum für Luft- und Raumfahrt (DLR), Institut für Physik der Atmosphäre, Oberpfaffenhofen, Germany*

Corresponding author: Wolfgang A. Müller, wolfgang.mueller@mpimet.mpg.de

https://doi.org/10.5194/egusphere-2025-2473
Preprint. Discussion started: 12 June 2025

Abstract. We develop a new Earth System model configuration framed into the ICON architecture, which provides the baseline for the next generation of climate predictions and projections (hereafter ICON XPP - where XPP stands for eXtended Predictions and Projections). ICON XPP is an outcome of a joint project between climate research institutes and the Deutscher Wetterdienst, integrating numerical weather prediction and Earth System modeling and prediction based on the ICON framework. ICON XPP comprises the atmospheric component as used for the numerical weather prediction (ICON NWP), the ICON ocean and land surface components, and an ensemble-variational data assimilation system, all adjusted to an Earth System model for pursuing climate research and operational climate forecasting. Here, two baseline configurations are presented, one with a 160 km atmosphere and a 40 km ocean resolution, and one with 80 km atmosphere and 20 km ocean resolution, and a first evaluation is pursued based on the CMIP DECK (Diagnostic, Evaluation and Characterization of Klima) experimentation framework. Emphasis is given to the basic assessment of their mean climate, trends and climate sensitivity, and key processes in the tropics and mid-latitudes are examined, which are of relevance for climate predictions.

ICON XPP is able to depict the basic properties of the coupled climate. The pre-industrial climate shows a balanced radiation budget at the top-of-atmosphere and a mean global near-surface temperature of about 13.8-14 °C. The ocean shows circulation strengths in the range of the observed values, such as the AMOC at 16-18 Sv and the flows through the common passages. The current climate is characterized by a trend in the global mean temperature of ~1.2 °C since the 1850s, close to what is found in reference datasets. At regional scale, however, the hydroclimate deviates strongly from observed conditions. For example, the inter-tropical convergence zone (ITCZ) is dominated by a double peak with a particular wet southern subtropical branch over the oceans. Further, the climate in the Southern Ocean is characterized by a strong positive mean bias, with the sea surface temperature too high up to 5 °C.

Key dynamical processes are presented, such as the El Niño/Southern Oscillation (ENSO) whose overall performance fits with the CMIP6-like coupled models. However, in the present configuration, the amplitude is ⅔ of the observed values, and the ENSO feedbacks are underestimated. Further, tropical waves and the Madden-Julian Oscillation are captured well, and spontaneous weak quasi-biennial oscillation is found in the 40 km atmosphere configuration. The atmospheric dynamics at the extra-tropics of both configurations is particularly noteworthy. ICON XPP exhibits a good representation of the jet stream position,

https://doi.org/10.5194/egusphere-2025-2473
Preprint. Discussion started: 12 June 2025

particularly in the northern extra-tropics. Closer investigations show that the influences of the transient momentum transports and their feedbacks on the jet stream are well reproduced in ICON XPP. Stratospheric dynamics further reveal a sufficiently strong polar vortex and an adequate number of sudden stratospheric warmings. A clear improvement is found for all processes for the higher-resolved configuration compared to the lower resolution. Overall, ICON XPP performs at a similar level in the tested climate simulations as climate models performed in CMIP6 and forms a good basis for application in the areas of climate forecasts and projections, as well as climate research.

1. Introduction

For more than a decade, the Max Planck Institute Earth System model (MPI-ESM) has been used for climate predictions and projections and climate research. Climate predictions (here spanning the time range from seasons to 10 years ahead) based on MPI-ESM provide reliable forecast skill (Marotzke et al., 2016) and are routinely operated by the Deutscher Wetterdienst (DWD, Fröhlich et al., 2020). Further, MPI-ESM contributed to previous phases of the Coupled Model Intercomparison Project (CMIP) through various configurations (e.g., Giorgetta et al., 2013, Jungclaus et al., 2013, Müller et al. 2018, Mauritsen et al. 2019, Gutjahr et al., 2019). However, MPI-ESM will no longer be supported, and has been substituted by the ICON (ICOsahedral Nonhydrostatic) model framework. Since 2020, a new modeling initiative integrating numerical weather forecast, climate predictions and climate projections based on the ICON framework (Müller et al., 2025). An outcome of this initiative is ICON XPP - where XPP stands for eXtended Predictions and Projections -, a newly developed coupled Earth System model configuration. ICON XPP will be the baseline for next generation climate predictions, and provides the model platform for the contribution to the CMIP7 (Dunne et al., 2025). Here, we present ICON XPP, from the design of the configurations to a first evaluation of the Earth System state based on the CMIP DECK (Diagnostic, Evaluation and Characterization of Klima) experimentation framework (Eyring et al., 2016). Special attention is given to monitoring certain aspects of the tropical and extra-tropical mean climate, and the stratosphere, including key modes of variability and their predictability, such as the El Niño/Southern Oscillation (ENSO), or the North Atlantic Oscillation (NAO).

ICON XPP builds upon accomplishments of previous ICON initiatives for the individual components (Zängl et al., 2015, Korn, 2017, Giorgetta et al., 2018, Nabel et al., 2020, Reick et

https://doi.org/10.5194/egusphere-2025-2473
Preprint. Discussion started: 12 June 2025

al., 2021, Schneck et al., 2022, Korn et al., 2022), and a fully-coupled Earth System model (Jungclaus et al., 2022). Although these configurations are based on the same dynamical core and code infrastructure of ICON, their sub-grid scale closure and parameterization differ and depend on whether they are used for weather or climate scales. The design of ICON XPP aims at integrating scales from weather to climate into a single model system. It is developed by combining some of the well-established numerical weather prediction (NWP) and climate model components, and by synchronization of the physical parameterizations among weather and climate timescales (Müller et al., 2025). ICON XPP consists of the atmospheric component used for operational weather forecasts at the DWD (ICON NWP), which has achieved superior quality of weather forecasting compared to previous NWP model generations, as well as the ICON ocean and sea-ice model (Korn et al., 2022) and the land component JSBACH (Reick et al., 2021) coupled to ICON NWP.

A central aim of ICON XPP is to substitute MPI-ESM for climate predictions, upcoming climate projections and provision of basic research on fundamental climate properties. Climate predictions with the MPI-ESM have demonstrated skill at various timescales from seasons to multiple decades. On seasonal timescales, MPI-ESM shows prediction skill for various dominant modes of climate variability such as the ENSO (Fröhlich et al., 2020) and NAO (Dobrynin et al. 2018, 2022), continental-scale temperature and precipitation patterns, and it is recently for machine learning methodologies to assess the occurrence of heat extremes over Europe (Beobide-Arsuaga et al. 2023). MPI-ESM has been also used for decadal climate predictions to achieve an operational workflow (Marotzke et al., 2016, Hettrich et al., 2021). The principal drivers, such as the near-term memory of the North Atlantic Ocean heat content, and the long-term trends of the external forcing have manifested the near-term climate predictions skills in MPI-ESM (i.e., Marotzke et al. 2016 and references therein). In addition, predictions skill is assessed for key processes, such as the Quasi-Biennial Oscillation (QBO, Pohlmann et al., 2013), storm tracks in the northern hemisphere extra-tropics (Kruschke et al., 2016, Schuster et al., 2019), and the NAO (Smith et al. 2020, Athanasiadis et al., 2020). Further, skill is found for climate impacts, such as continental-scale surface temperature (Müller et al., 2012) and associated extremes (Borchert et al., 2019), and Earth System components, such as the carbon uptake in the ocean (Li et al. 2016). Recently, MPI-ESM has been used to extend the prediction skill to a multi-decadal timescale (Düsterhus and Brune, 2023). A principal ambition is that ICON XPP is able to cover predictions at all timescales from months to

https://doi.org/10.5194/egusphere-2025-2473
Preprint. Discussion started: 12 June 2025

centennials. Given these targets, special emphasis is put on incorporating and improving model components particularly suitable for climate predictions. Though this attempt is quite broad, first initiatives led to the inclusion of a higher-resolving stratosphere, and special attention was paid to the key properties in the tropics and the extra-tropics.

While designing ICON XPP, we paid attention to fast and flexible model configurations, to perform long integrations and large ensembles, in contrast to current high-resolution ICON model initiatives. Long-time integrations are particularly useful while testing the parameter space finding an equilibrium state of the coupled system, but also for probing the ideal setting for improving key dynamics. Large ensembles are the standard procedure in simulations of climate projections, and to assess reliability in the ensemble forecasts and eventually to improve the signal-to-noise ratio by adequate methodologies (Dobrynin et al., 2018, Smith et al., 2019). Further, large ensembles are essential for the assessment of the transient climate variability (Maher et al., 2019). The ICON XPP configurations presented here are designed to run several simulated decades per day and are suitable for the aforementioned tasks.

While the development and evaluation of ICON XPP for operational climate prediction and CMIP7 is still in progress, here we present its principal development lines and fundamental properties of the coupled Earth System state. We use the DECK-experimental design - which has been developed as a guideline to improve and compare coupled Earth System models (Eyring et al., 2016) - and apply it to different ICON XPP configurations. We present the basic model description and ways towards tuning the model climate, followed by an evaluation of the basic climate state, trends, and climate sensitivity in the DECK experiments.

2. Model Description, Configurations, and Tuning

2.1 Model Components

ICON XPP combines Earth System components that have been established for operational weather forecasting and climate application, and here are plugged together for the first time. In the following, the components that form ICON XPP are described in more detail.

ICON NWP

https://doi.org/10.5194/egusphere-2025-2473
Preprint. Discussion started: 12 June 2025

The atmospheric component of ICON XPP is based on the operational configuration of ICON NWP (Zängl et al. 2015). In ICON NWP, the basic non-hydrostatic model equation system is solved on a triangular grid. The vertical grid of ICON is a terrain-following hybrid sigma height grid (Leuenberger et al., 2010, Giorgetta et al., 2018), with a model top at 75 km. The centerpiece is the dynamical core, in which the model equations are integrated forward in time, followed by the numerical advection schemes and physical parameterizations (for details see, Prill et al., 2024). ICON NWP uses the physics packages from the operational regional model COSMO (Doms and Schättler, 2004), and from the ECMWF Integrated Forecast System (Zängl et al. 2015). For radiation, the ecRad scheme is used in ICON NWP (Hogan and Bozzo, 2018). An overview of the physical parameterizations is given in Müller et al. (2025, Table 1).

ICON Land

ICON XPP uses the land surface component of ICON (ICON Land). ICON Land uses the JSBACH land-surface model developed for predecessors of ICON XPP such as MPI-ESM (Reick et al., 2013, 2021). JSBACH version 3 (JSBACHv3) operated as a part of MPI-ESM in both, concentration and emission-driven modes, and demonstrated good performance of terrestrial carbon cycle in CMIP6 (Hajima et al., 2024). JSBACH version 4 (JSBACHv4) includes climate-relevant physical and biogeochemical processes, such as a full carbon cycle, dynamic vegetation, and land-cover changes for land use. In addition, soil physics in JSBACHv4 are improved in permafrost regions compared to JSBACHv3. The land surface model can be used in stand-alone mode, as well as in the fully coupled Earth System models (Jungclaus et al., 2022).

For ICON XPP, JSBACH is newly implemented together with its parameterization of the vertical diffusion as an implicitly coupled module of ICON NWP. As TERRA, JSBACH accounts for subgrid heterogeneity. However, in contrast to TERRA, in which tiles are treated externally, JSBACH uses them internally to account for different land surface types and plant functional types (PFTs) as a basis for biogeochemical processes. Therefore, a new interface layer is developed between JSBACH, its vertical diffusion scheme, and the rest of the NWP parameterizations. This new interface layer results in the adjustment of code for other sub-components. For example, parts of the sea-ice thermodynamics scheme are re-implemented, and the coupling to the ocean is generalized.

https://doi.org/10.5194/egusphere-2025-2473
Preprint. Discussion started: 12 June 2025

Hydrological Discharge Model

A hydrological discharge (HD) model is used in ICON XPP to route water from the land model JSBACH to the river mouths feeding into the ocean model ICON O. In ICON XPP we can choose between two HD model versions. One is the internal HD model integrated within JSBACH. This HD model operates at the same horizontal resolution and time step as JSBACH, maintaining coherence between land and hydrological processes. Automatic generation of HD parameters for ICON grids based on high resolution digital elevation data (Riddick et al., 2018, Riddick, 2021) allows HD application on any spatial resolution using none or minimal manual adjustments. This model is used for ICON XPP in the fast configuration (see section 2.2).

For the higher-resolved ICON XPP configuration, a new version of the HD model with relatively high resolution of 0.5° is used externally to JSBACH (Hagemann et al., 2023). It is a separate component coupled via YAC (Yet Another Coupler, Hanke et al., 2016) with both the land-surface and the ocean model component. In this setup, the 0.5-degree HD model is coupled to the atmosphere and the ocean with daily intervals. The land-surface scheme from ICON NWP handles surface and subsurface runoff, which are interpolated by YAC onto the HD latitude-longitude grid. This approach offers the advantage of being independent of the land model, allowing HD to work with other land models such as TERRA. It will also easily allow future applications using the HD model at its higher resolution of 1/12° (Hagemann et al. 2020), and taking advantage of ongoing developments in riverine transport of biogeochemical tracers (e.g. Elizalde et al. 2025).

ICON O/Sea-Ice

The ocean component of ICON solves the hydrostatic Boussinesq equations of large-scale ocean dynamics with a free surface (Korn, 2017, Korn et al., 2022). ICON O uses the same horizontal grid and data structures as the atmosphere. For the vertical grid, the actual model uses depth-based coordinates such as z or z*-coordinates as the default option (Korn et al., 2022). For ICON XPP, we use the uniformly vertical-distributed grid with the z*-coordinate. Further, a newly developed sea-ice dynamics is applied that operates on the native ICON grid (Mehlmann and Korn, 2021, Mehlmann et al., 2021). The sea-ice thermodynamics are unchanged and continue to use the zero-layer model (Semtner, 1976). At the bottom, melting potential and conductive heat flux are passed to dynamic sea-ice components by use of the YAC coupler.

https://doi.org/10.5194/egusphere-2025-2473
Preprint. Discussion started: 12 June 2025

HAMOCC

The ocean biogeochemistry component in ICON XPP is represented by the HAMburg Ocean Carbon Cycle model, HAMOCC6 (Ilyina et al., 2013, Paulsen et al., 2017), featuring biology and inorganic carbon chemistry processes in the water column and sediment. The growth of bulk phytoplankton is limited by temperature and light as well as by the availability of nutrients including nitrate, phosphate, and iron linked by constant Redfield ratios across organic compartments. The growth of nitrogen-fixing cyanobacteria is parameterized analogously to that of the bulk phytoplankton, albeit at a lower rate and is extended by representing their buoyancy. Detritus is explicitly separated into opal- and calcium carbonate-producing phytoplankton fractions. Zooplankton growth function is limited by the grazed phytoplankton, mortality, and metabolic activity. The dissolved organic matter pool is shaped by the exudation of phytoplankton, cyanobacteria, and zooplankton. All the biogeochemical tracers are transported by the flow field. HAMOCC has been extensively evaluated as part of MPI-ESM (e.g. Mauritsen et al., 2019; Müller et al., 2018; Li et al., 2023; Nielsen et al., 2024) and implemented in previous configurations of the ICON-based models (Jungclaus et al., 2022; Hohenegger et al., 2023). Compared to its predecessors, HAMOCC in ICON XPP incorporates a prognostic calculation for marine aggregate sinking speeds (Maerz et al., 2020), providing an improved distribution of particulate organic carbon fluxes critical to the ocean biological pump.

2.2 Configuration

We use the latest ICON model version (ICON release 2024.07). Two configurations have been developed, differing mainly in spatial resolutions. One configuration, intended for operational climate prediction and projections, utilizes the atmospheric model ICON NWP with approximately 80 km horizontal grid spacing (r2b5) and 130 vertical levels (L130, Niemeier et al, 2024). The vertical spacing of the layers increases up to a value of 500 m at an altitude of about 14 km and stays constant (500 m) until an altitude of 35 km. Above this height the vertical distance increases until the model top at 75 km altitude (Fig. 1). This configuration uses the externally calculated HD model as described above. The ocean model operates at a resolution of about 20 km (r2b7) with 72 vertical levels (L72). The integration time steps for ICON NWP and ICON O are 450 seconds and 20 minutes, respectively. The coupling interval between the atmosphere and ocean is 60 minutes. Due to its high resolution and frequent computation intervals, this configuration is computationally expensive, but a throughput of ~45 simulated

https://doi.org/10.5194/egusphere-2025-2473
Preprint. Discussion started: 12 June 2025

years per day on 100 nodes ensures long integrations. The experiments are run on the CPU-partition of a High-Performance Computing system at the Deutsche Klimarechenzentrum (DKRZ), with each node consisting of 64 cores. This configuration is named "80/20" hereafter to reflect the grid-scale of the atmospheric and ocean components.

In addition, a fast configuration with coarser resolutions was developed to allow more efficient simulations. In this configuration ICON NWP is run with a 160 km grid (r2b4) with 90 vertical levels (L90) and model top at 75 km, while ICON O operates on a 40 km grid (r2b6). The HD model is implemented internally to JSBACH. Additionally, the ocean model's time step is increased as compared to the 80/20 configuration to 30 minutes. The coupling interval between the atmosphere and ocean is 30 minutes for this configuration. This faster configuration is designed for running large ensembles and long integrations and has a throughput of ~85 simulated years per day on 40 computing nodes. This configuration is referred to as "160/40" hereafter.

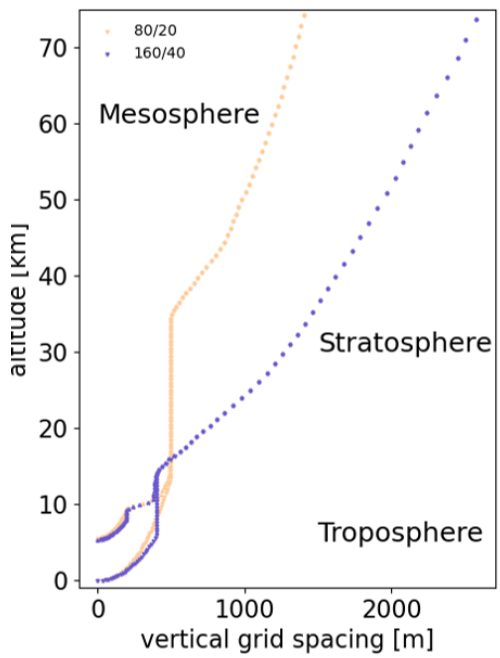

Figure 1: Full-level height (km) and vertical grid spacing (m) of the vertical grids of ICON XPP 160/40 and 80/20. For each grid two profiles are shown, one starts at sea level (triangle down) and one starts at a height of ~ 5 km representing the grid over mountains (triangle up).

https://doi.org/10.5194/egusphere-2025-2473
Preprint. Discussion started: 12 June 2025

2.3 Tuning

The model configurations are tuned towards pre-industrial climate targets. The targets mainly consider the thermodynamic state of the atmosphere - depicted by the top-of-atmosphere radiation balance and global-mean temperature at 2 metre - and the ocean-cryosphere - by the strength of the Atlantic meridional overturning circulation (AMOC) and sea-ice properties. The thermodynamic state of the atmosphere is mainly controlled by parameters in the convection, microphysics and cloud cover parameterization schemes. The ocean state is controlled by the horizontal and vertical diffusion, eddy parameterizations, and sea-ice parameters (Table 1).

The spin-up is started from the Polar Science Center hydrographic climatology (PHC3.0, Steele et al., 2001). The top of the atmosphere (TOA) radiation values are well-balanced with values of 0.2 W/m^2 (-0.1 W/m^2) for the 160/40 (80/20) configuration. A global mean near-surface temperature (GMT) of ~13.8 °C is achieved for both configurations. Figures 2a and 2b show the evolution of the radiation and GMT. The figures illustrate that the atmosphere reaches quasi-equilibrium after ~200 years, despite small trends towards lower temperatures remaining at the end of the simulations. The ocean state is also well-balanced as indicated by the AMOC @26° N and 1000 m depth (Fig. 2c), but requires ~500-600 years to reach equilibrium. In 160/40 a small trend remains for the AMOC at the end of the simulation.

The tuning of the ocean biogeochemistry is carried out after the spin-up of the coupled configuration. The target is to limit drifts in the biogeochemical tracer fields and fluxes and to drive the model closer to observations. HAMOCC tracers are initialized from a tuned stand-alone 40 km ocean setup, which was spun up for ~1000 years in a pre-industrial climate. The HAMOCC tuning parameters were changed accounting for the ocean circulation in the coupled model. The appropriate weathering rates were updated during the simulation, to compensate for the loss of carbon and nutrients from the water column to the sediment,.

Parameter Values	Process	160km/40km	80km/20km	Default
ICON NWP				
Entrainment rate [m^{-1}] **(tune_entrorg)**	Convection	0.0021	0.0028	0.00195

https://doi.org/10.5194/egusphere-2025-2473
Preprint. Discussion started: 12 June 2025

Cloud cover parameter (tune_box_liq_asy)	Cloud microphysics	3.35	3.6	2.5
Turbulent diffusion (f_theta_decay)	Vertical diffusion	1.0	1.0	4.0
ICON O				
TKE mixing (c_k)	Vertical diffusion	0.05	0.1	0.1
Minimum interior mixing [m^2s^{-2}] **(tke_min)**	Vertical diffusion	1.0e-5	1.0e-6	1.0e-6
Biharmonic Viscosity Parameter [m^4s^{-1}]	Horizontal velocity diffusion	3.5e12 (no scaling)	0.027 (scaling with edge length)	/
Gent&McWilliams [m^2s^{-1}] **(tracer_GM_kappa)**	Eddy Parameterization	400	400	1000 (corresp. to 400 km grid-length)
Redi [m^2s^{-1}] **(tracer_isoneutral)**	Eddy Parameterization	400	400	1000 (corresp. to 400 km grid-length)
Sea ice parameter (leadclose1)	Sea ice melting	0.25	0.25	0.5
Sea ice parameter (leadclose2)	Sea ice freezing	0.666	0.0	0.0 (Hibler)

Table 1: Parameter values used for tuning the ICON XPP configuration towards the pre-industrial climate targets. The table only shows parameters which values differ with respect to the ICON NWP and ICON O default values. The default for ICON NWP and ICON O is related to the ICON release (2024.07) and the namelist document therein.

https://doi.org/10.5194/egusphere-2025-2473
Preprint. Discussion started: 12 June 2025

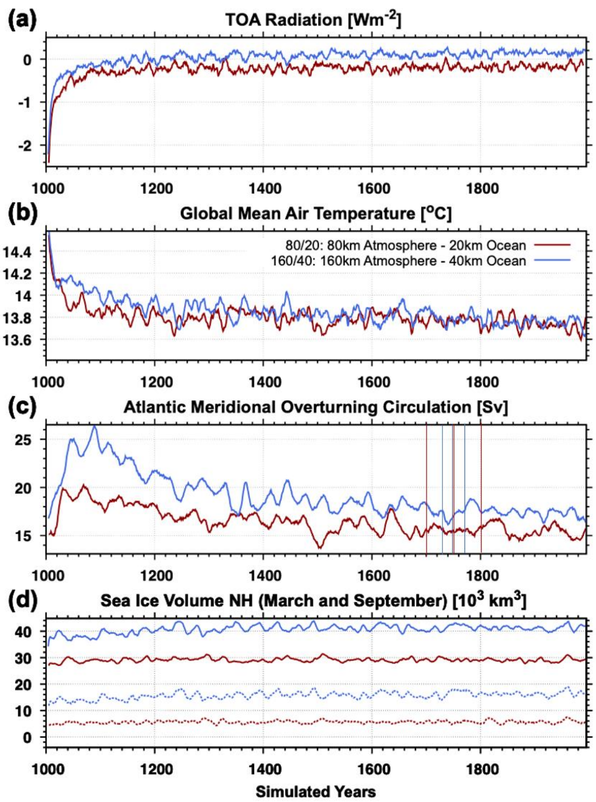

Figure 2: Climate equilibrium in CTRL indicated by the evolution of (a) TOA net radiation, (b) GMT, (c) Atlantic meridional overturning circulation, and (d) the northern hemisphere sea-ice volume. Units are in (a) W m^{-2}, (b) °C, (c) Sv, and (d) km^3. In each figure 80/20 is shown in red and 160/40 is shown in blue. The vertical lines in (c) indicate the initialization dates for HIST. In (d) solid/dashed lines represent northern hemispheric winter/summer.

3. Mean Climate, Trends and Climate Sensitivity

3.1 DECK Experiments

We perform DECK experiments, which have become a common tool for coordinating a comparable design of global climate model simulations (Eyring et al., 2016). Pre-industrial control simulations (CTRL) for each configuration are performed based on the spin-up experiments. For each configuration a spin-up and CTRL of total length of 1000 years are pursued. Further, ensembles of experiments with historical forcing from CMIP6 (HIST) are

https://doi.org/10.5194/egusphere-2025-2473
Preprint. Discussion started: 12 June 2025

used to analyse the present-day evolution of climate. The initial conditions for the historical experiments are based on the coupled control climate with a 50-year lag for subsequent members. Finally, the climate sensitivity is estimated by 1% CO_2 increase until doubling (1%CO_2) and abrupt 4 x CO_2 (4xCO_2) experiments. Table 2 gives an experiment overview.

Experiment List	Description	Number of simulated years
Spin-up and pre-industrial control simulation (CTRL)	Started from Levitus and external forcing only	1000
Historical simulation (HIST)	Started from CTRL with transient external forcing, 3 ensemble members	1850-2014
1% increase of CO_2 (1%CO_2)	Atmospheric CO_2 concentration prescribed to increase at 1 % yr^{-1}	150
4x abrupt CO_2 (4xCO_2)	Atmospheric CO_2 concentration abruptly quadrupled and then held constant	150

Table 2: List of experiments, short description and number of simulated years of DECK experiments for both configurations.

3.2 Pre-industrial Control Climate

The CTRL experiments reveal bias distributions well-known in coupled climate models. Near-surface temperatures in both configurations exhibit warm biases in the upwelling region at the coastal western boundaries (Fig. 3). A cold tongue is visible in both configurations in the tropical Pacific, and a further cold bias hot spot is found along the North Atlantic Current. The Southern Ocean marks an area with a very pronounced warm bias up to 5 °C (3 °C) in 160/40 (80/20), which appear relatively large compared to the CMIP6 multi-model mean (2-2.5K, Luo et al. 2023) and the previous model generations (Müller et al., 2018, Jungclaus et al., 2022). Preliminary analysis of the sources of these biases point towards a too deep ocean mixed layer in the Weddell Sea associated with strong vertical mixing (not shown). In addition, the atmosphere reveals a strong short-wave net radiation bias over the Southern Ocean, which is related to the appearance of too few clouds. The cloud bias is also found in an AMIP-type simulation and reveals that in this area the clouds comprise too little cloud water and too much cloud ice. To disentangle the atmospheric and oceanic effects on the Southern Ocean bias is

https://doi.org/10.5194/egusphere-2025-2473
Preprint. Discussion started: 12 June 2025

still under investigation. The global standard deviation of the error is ~2.4 °C for 160/40 and ~1.7 °C 80/20, which indicates a substantial effect by the resolution increase. Such a resolution effect on the mean error is also found in the MPI-ESM (Müller et al., 2018).

The sea-ice reveal reasonable distributions in the northern hemisphere peak season with 2-3 m sea-ice thickness in the central Arctic and 0.1-0.2 m within the Labrador Sea (Fig. 4, shown only for 80/20, but similar in 160/40). During the minimum seasons in the northern and southern hemisphere both configurations show only little sea-ice thickness. The sea-ice volume of 80/20 in the peak seasons is about 30 x 10^3 km^3 in the northern hemisphere (Fig. 2d), which is comparable with the PIOMAS arctic sea-ice volume reanalysis (30-35 x 10^3 km^3 April value during 1980s; Zhang and Rothrock, 2003), and 13 x 10^3 km^3 in the southern hemisphere (not shown). During hemispheric summer seasons the sea-ice volume drops to 5 x 10^3 km^3 in the Arctic (PIOMAS ~15 x 10^3 km^3 September values during the 1980s, Schweiger et al., 2011) and 0.5 x 10^3 km^3 in the Antarctic region. The 160/40 configuration generally produces much more sea ice compared to 80/20 (Fig. 2d red curves), which can also be inferred from the surface temperatures in high latitudes (Fig. 3a).

The state of the ocean circulation of the two configurations is described by the overturning circulations in the Atlantic and Indo-Pacific (Fig. 5) and transport through various passages (table 3). The overturning in the Atlantic shows peak magnitudes of ~15-20 Sv at 26° N at 1000 m depth, which is comparable to the RAPID array (~17 +/-4 Sv, Frajka-Williams et al., 2019). The two configurations show a monocell structure with a northward transport of water masses in upper and mid-levels and southward transport in deeper levels. In the Pacific, the surface values indicate the subtropical cells at the northern and southern hemisphere. At deeper levels a basin-wide mid-depth outflow occurs in both configurations.

The transports through the passages in both configurations are mostly simulated within the observational uncertainty found in the literature (see table 3 for values and references). The transport through Bering Strait - a key element of the Arctic freshwater budget, are close to the estimates by Woodgate et al. (2006, 2012). The exchange of water masses between the Atlantic Ocean and the Nordic Seas plays a vital role in driving the global overturning circulation. The simulated transport rates are consistent with the circulation pattern described by Hansen et al. (2008). Similarly, the Indonesian Throughflow is a key component of the warm-water branch of the global conveyor belt. Although the simulated transport in this region is slightly underestimated compared to the values reported by Gordon et al. (2010), it still aligns

https://doi.org/10.5194/egusphere-2025-2473
Preprint. Discussion started: 12 June 2025

reasonably well with observational estimates. These transports are similar to what is found in MPI-ESM (cf Table 5 in Müller et al., 2018) and ICON-ESM (cf Table 4 in Jungclaus et al., 2022). The Drake Passage transport is notably underestimated in 80/20, both when compared to the traditional estimate of around 135 Sv (Cunningham et al., 2003; Nowlin & Klinck, 1986) and to the more recent compilation by Donohue et al. (2016).

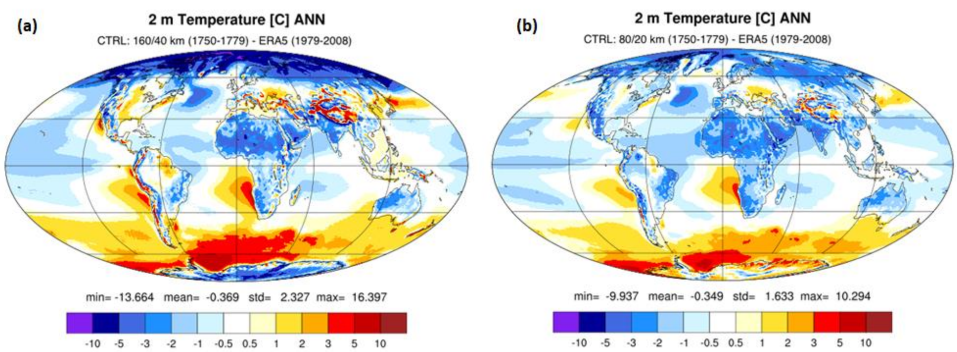

Figure 3: Near-surface temperature bias for a 30-year time slice for CTRL for (a) 160/40 and (b) 80/20. As reference ERA5 for the period 1979-2008 is used. Units are [°C].

https://doi.org/10.5194/egusphere-2025-2473
Preprint. Discussion started: 12 June 2025

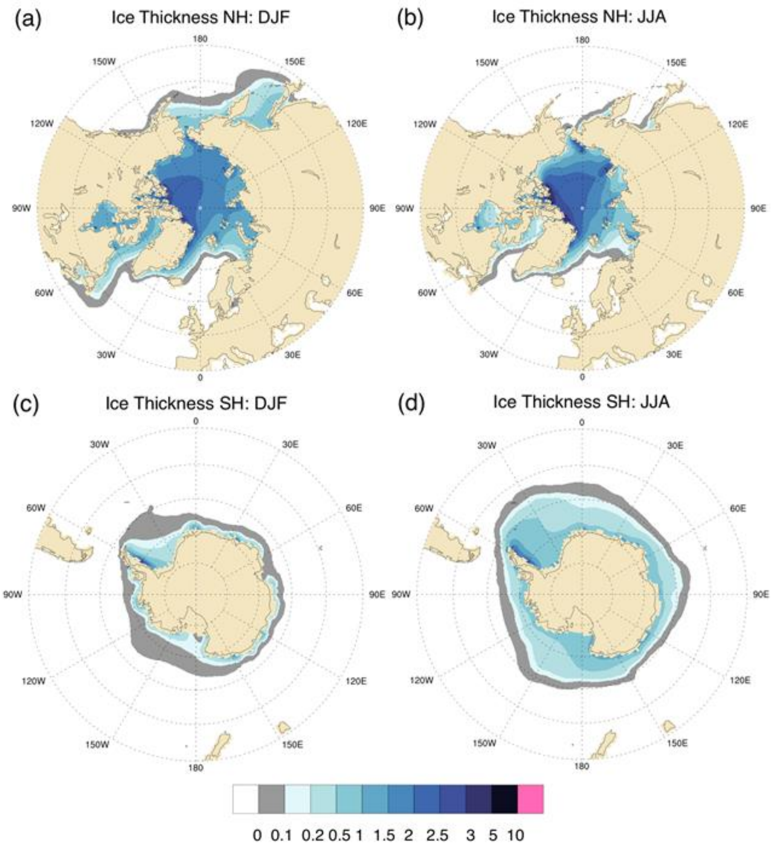

Figure 4: Sea-ice thickness for 80/20 for (a, b) the northern and (c, d) southern hemisphere for (a, c) December, January, February (DJF) and (b, d) June, July, August (JJA) for 80/20. The same 30-year timeslice of CTRL as in figure 3 is used. Units are in [m].

https://doi.org/10.5194/egusphere-2025-2473
Preprint. Discussion started: 12 June 2025

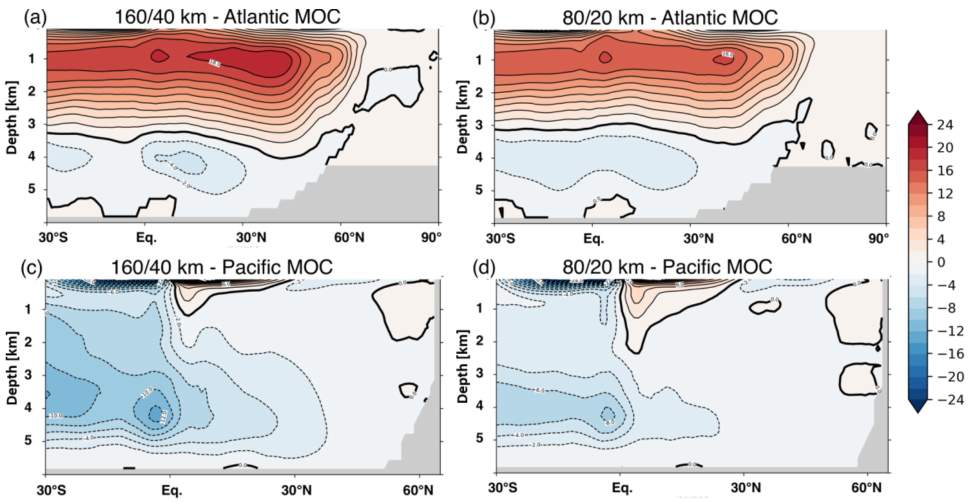

Figure 5: The overturning circulation in the Atlantic (a,b) and Indio-Pacific (c,d) for 160/40 (a,c) and 80/20 (b,d). For both, the same 30-year timeslice of CTRL as Figure 3 is used. Units are in Sverdrup [10^9 kg s^{-1}].

The ocean biogeochemistry for the 80/20 configuration is shown in Fig. 6, depicting the phosphate, total alkalinity, and dissolved inorganic carbon (DIC) at the surface compared to the Global Ocean Data Analysis Project (GLODAP) version 2 database (Olsen et al. 2016). The spatial patterns of biogeochemistry fields are captured, with bias patterns similar to other Earth System models and previous ICON-ESM simulations (Jungclaus et al. 2022). Surface phosphate is underestimated in the eastern equatorial Pacific and Southern Ocean, and overestimated along the southern Chilean coast. The bias in surface alkalinity and DIC is relatively small in most regions, with higher biases observed in coastal regions due to under-representation of coastal carbon dynamics (Mathis et al. 2022). The global pattern of surface alkalinity bias follows the bias in sea-surface salinity, with negative salinity bias leading to negative alkalinity bias. Since the model is forced with constant pre-industrial atmosphere CO_2, the surface DIC in the model adjusts to the surface alkalinity. Therefore, bias in surface alkalinity is compensated by bias in surface DIC, maintaining a correct ocean pCO_2 field. The simulated global flux of CO_2 into the ocean is approximately 0.1 PgC/year, close to the equilibrium levels at pre-industrial conditions.

https://doi.org/10.5194/egusphere-2025-2473
Preprint. Discussion started: 12 June 2025

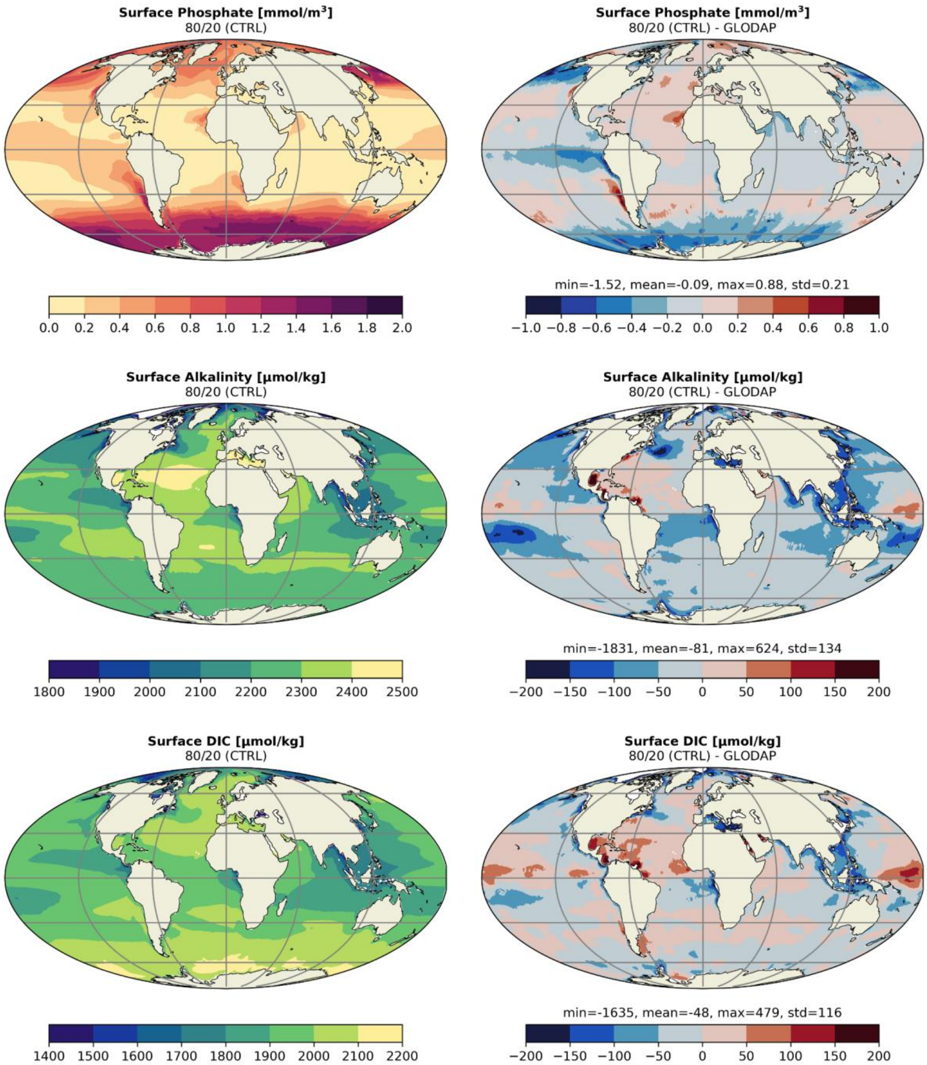

Figure 6: Simulated phosphate (upper), alkalinity (middle) and DIC at the surface (lower) for 80/20 climatology (left) and corresponding difference to reference data from the Global Ocean Data Analysis Project version 2 database (right). The GLODAP phosphate and alkalinity are climatological means and the DIC is from pre-industrial estimates. The analysis is based on a 30-year time window of the CTRL experiment.

The performance of the land carbon model is illustrated by a plot of gross primary productivity (GPP) for CTRL simulations in the 160/40 and 80/20 configurations (Fig. 7). The spatial GPP patterns in both configurations look very similar, with tropical productivity being much higher

https://doi.org/10.5194/egusphere-2025-2473
Preprint. Discussion started: 12 June 2025

than extra-tropical productivity, as expected. The patterns reflect the simulated biases in tropical precipitation (e.g., over eastern and central South America), but are otherwise very similar to the pattern simulated with MPI-ESM in CMIP6. The total annual productivity fluxes are 114.5 ± 1.8 PgCyr-1 and 112.9 ± 1.6 PgCyr-1 in the 160/40 configuration and the 80/20 configuration, respectively. Both model configurations are well within the CMIP6 model range for the pre-industrial period and close to the AR6 estimate of pre-industrial GPP in 113 PgCyr-1 (Canadell, J.G., et al., 2021).

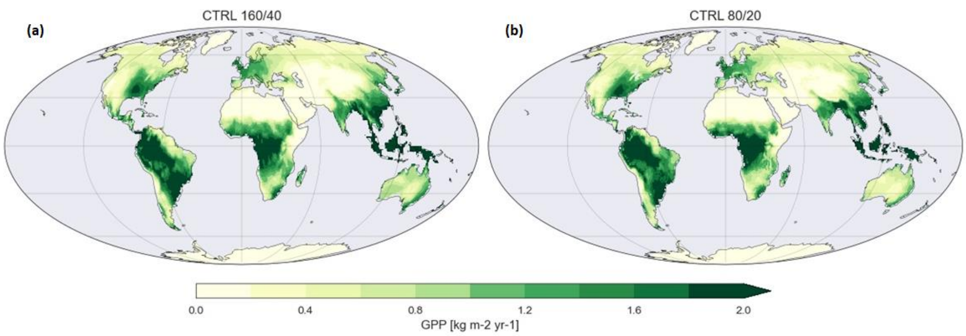

Figure 7: 30-years mean of yearly accumulated gross primary productivity for CTRL of ICON XPP in the (a) 160/40 and (b) 80/20 configurations.

https://doi.org/10.5194/egusphere-2025-2473
Preprint. Discussion started: 12 June 2025

Experiment List	160/40	80/20	Observations
Bering Strait [Woodgate et al. (2006) and Woodgate et al. (2012)]	1.0	1.1	0.7–1.1
Fram Strait [Fieg et al. (2010)]	-1.5	-2.0	-1.75 ± 5.01
Denmark Strait [Hansen et al. (2008); Jochumsen et al. (2012)]	-5.0	-5.2	-4.8; -3.4 ± 1.4
Iceland-Scotland [Hansen et al. (2008); Rossby and Flagg (2012)]	4.9	5.1	4.8; 4.6 ± 0.25
Indonesian Throughflow [Gordon et al. (2010)]	12.4	12	11.6–15.7
Drake Passage [Nowlin and Klinck (1986); Donohue et al. (2016)]	152.1	111	134.0 ± 14.0; 173.3 ± 10.7

Table 3: Simulated and observed net volume transports across sections (positive means northward). Units are in [Sv].

3.3 Transient Climate - 1850 to present

To recreate the climate of the historical period from 1850 to present, we employed external forcings from CMIP6, as the CMIP7 input data were not yet available at the time of these experiments. Specifically, we included yearly anthropogenic land cover changes, volcanic aerosol, and anthropogenic aerosol, which were added to the baseline aerosol concentrations

https://doi.org/10.5194/egusphere-2025-2473
Preprint. Discussion started: 12 June 2025

of the pre-industrial period. Additionally, monthly ozone data and annual greenhouse gas concentrations were incorporated to reflect the evolving atmospheric composition over time.

All experiments were conducted using the tuned namelist parameters derived from the CTRL experiments (see Section 3.2). For each of the configurations, a small ensemble of three members was generated. Each ensemble member was initialized from the corresponding CTRL experiment. The members differ only in their starting points, which were selected from various time points with the distance of 50 (160/80) and 25 years (80/20) apart in the CTRL period.

Figure 8 shows the temporal evolution of GMT and global mean total precipitation. The development of GMT is close to observations from the 1960s onwards, and in the 2010s is about ~1.2 °C above 1850-1900. The increase is in the range of observed warming of 0.9-1.2 °C (Gulev et al., 2021). The global mean total precipitation shows a substantial positive bias in both configurations compared to GPCP and ERA5, and is on the upper end of all CMIP6 models. The global distribution of the bias reveals a strong double-ITCZ in the tropical Pacific with values up to 6 mm/day within the southern hemispheric branch, and particularly high values in the tropical Atlantic. Over the tropical continental regions strong dry bias occurs, such as in the Amazon and over Indonesia. The precipitation bias in the tropical Pacific imposes a limitation for the global climate because it covers a large region of the globe in a rain-dominated area. The causes are currently unclear, and further investigations are in progress.

In addition, we show the vertical temperature bias of the two configurations (Fig. 9). The bias structures are characterized by cold biases of the tropical atmosphere above the boundary layers, cold biases at tropopause levels, and warm biases at the surface in the high latitudes. The tropical cold bias reaches up to -1 °C in the 160/40 configuration accompanied with upper-level positive biases in the sub-tropics. The cold bias in 80/20 is increased up to -2 °C and reaches the sub-tropical regions. The positive surface bias is relatively large over the Southern Hemisphere with values up to 5 °C in both configurations and are in line with surface temperature distribution in Figure 3.

A summary of the model performance is given in Figure 10, which compares several key dynamical and thermodynamic variables with the CMIP6 model ensemble. A clear shift towards smaller errors is found by increasing the resolution from the 160/40 to the 80/20 configuration. A similar impact of resolution is found for previous model versions, such as for MPI-ESM (Müller et al., 2018). Exceptions to the reduction of RMSE with resolution are variables describing the cloud properties and liquid water path, which underlines a systematic

https://doi.org/10.5194/egusphere-2025-2473
Preprint. Discussion started: 12 June 2025

bias in the configurations with respect to the long-term mean hydrosphere. The 80/20 ensemble, however, exhibits a relatively strong performance among the CMIP6 models for dynamical variables, such as zonal wind and temperatures in the mid- and upper troposphere.

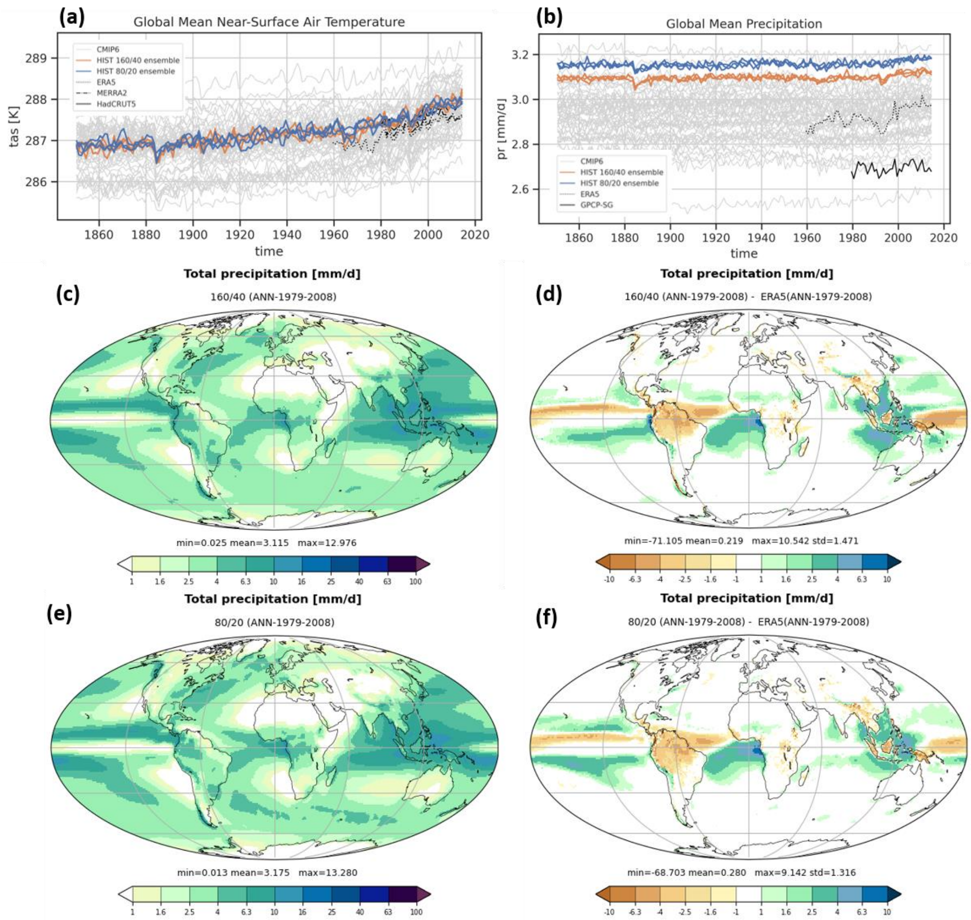

Figure 8 Evolution of (a) the global mean near-surface temperature (Kelvin) and (b) the global mean total precipitation (mm day^{-1}) from the three historical ensembles HIST for the 160/40 (orange) and the 80/20 configuration (blue). The evolutions are compared with CMIP6 models (grey) and respective observations/reanalyses (black). Geographical distribution of absolute values of (c, e) total precipitation and (d, f) precipitation bias with respect to ERA5 for one member of the (c, d) 160/40 and (e, f) 80/20 configuration, averaged for the period 1979-2008 both in (mm/day). Details on reference data sets are given in Table 4.

https://doi.org/10.5194/egusphere-2025-2473
Preprint. Discussion started: 12 June 2025

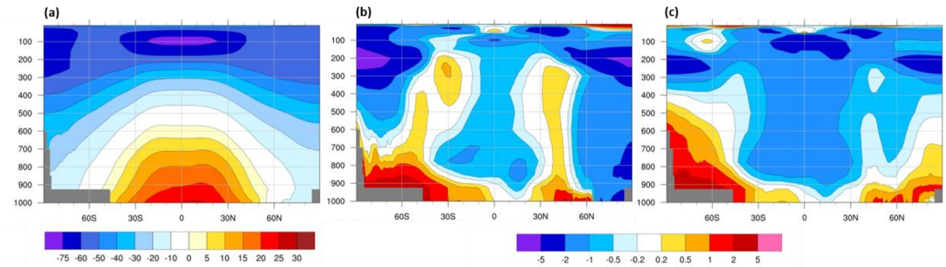

Figure 9: (a) Annual man zonal mean temperature in the troposphere for the period 1979-2008 for ERA5 and biases for HIST for one member of the (b) 160/40 and (c) 80/20 resolutions. Units are [°C].

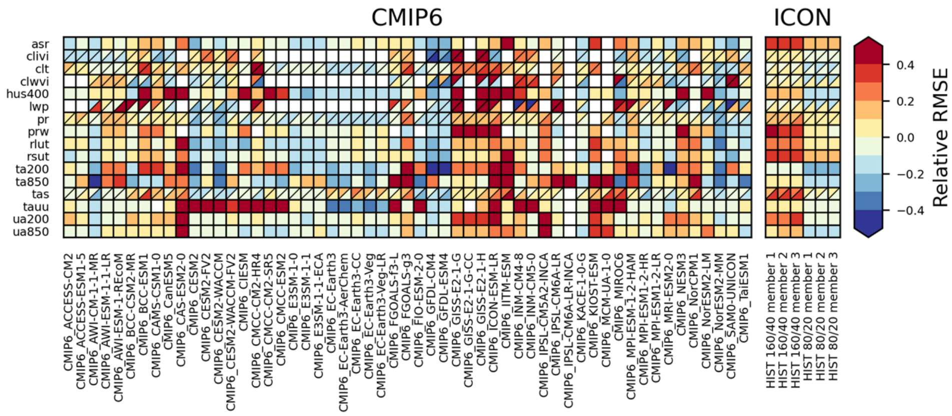

Figure 10: The performance matrix for the 160/40 and 80/20 resolutions (rightmost columns) and CMIP6 models (left columns) for key dynamical and thermodynamic variables. Shown are normalized relative space–time root mean square errors (RMSEs) of the climatological seasonal cycle with respect to reference observational data sets. The normalization is done relative to the ensemble median of all models, with positive values (red) denoting a higher RMSE and thus worse performance, while negative values (blue) denote a lower RMSE than the ensemble median and thus a better performance. The considered time period is 2000-2014 for the models, for the observational reference data the time period had to be adjusted to the available time frame (see Table 4 for details). Boxes with a diagonal split indicate that two different reference data sets are used, with the first mentioned reference in the top left corner. The variables shown are the absorbed solar radiation (asr; reference: CERES-EBAF), ice water path (clivi; references: ESACCI-CLOUD, MODIS), total cloud cover (clt; references: ESACCI-CLOUD, PATMOS-x), condensed water path (clwvi; references: MODIS, ESACCI-CLOUD), specific humidity at 400hPa (hus400; reference: ERA5), liquid water path (lwp; references: ESACCI-CLOUD, MODIS), total precipitation (pr; references: GPCP-SG, ERA5), water vapor path (prw; reference: ESACCI-WATERVAPOUR), TOA outgoing longwave radiation (rlut; reference: CERES-EBAF), TOA outgoing shortwave radiation (rsut; reference: CERES-EBAF), temperature at 200 hPa (ta200; reference: ERA5) and 850 hPa (ta850; reference: ERA5), surface temperature (tas; references: HadCRUT5, ERA5), zonal wind stress (tauu; reference: ERA5), and zonal wind at 200 hPa (ua200; reference: ERA5) and 850hPa (ua850; reference: ERA5).

https://doi.org/10.5194/egusphere-2025-2473
Preprint. Discussion started: 12 June 2025

Reference data sets	Type	Variables	Time range used in Figure 7	Reference
CERES-EBAF Ed4.2	Satellite	Absorbed solar radiation (asr) TOA outgoing longwave radiation (rlut) TOA outgoing shortwave radiation (rsut)	2001-2014	Loeb et al. (2018)
ERA5	Reanalysis	Specific humidity (hus) Total precipitation (pr) Air temperature (ta) Near-surface air temperature (tas) Zonal wind stress (tauu) Zonal wind (ua)	2000-2014	Hersbach et al. (2020)
ESACCI-CLOUD	Satellite	Ice water path (clivi) Condensed water path (clwvi) Total cloud cover (clt) Liquid water path (lwp)	2000-2014	Stengel et al. (2020)
ESACCI-WATERVAPOUR	Satellite	Water vapor path (prw)	2003-2014	Schröder et al. (2023)
GPCP-SG v2.3	Satellite - gauge	Precipitation (pr)	2000-2014	Adler et al. (2017)
HadCRUT5 v5.0.1.0 (analysis)	Ground	Near-surface air temperature (tas)	2000-2014	Morice et al. (2021)
MERRA2	Reanalysis	Near-surface air temperature (tas)	Not used	Gelaro et al. (2017)
MODIS	Satellite	Ice water path (clivi) Condensed water path (clwvi) Liquid water path (lwp)	2003-2014	Platnick et al. (2003)
PATMOS-x	Satellite	Total cloud cover (clt)	2000-2014	Heidinger et al. (2014)

Table 4: Observational reference data sets used in Fig. 7.

3.4 Climate Sensitivity

Climate sensitivity describes the response of the climate system to radiative forcing and is a key indicator for future evolution of climate. Two metrics are commonly used: the transient climate response (TCR) and the equilibrium climate sensitivity (ECS).

https://doi.org/10.5194/egusphere-2025-2473
Preprint. Discussion started: 12 June 2025

TCR is determined from the 1%CO_2 experiment as the global mean surface air temperature increases (relative to the CTRL experiment) around the time of doubling CO_2. Following Meehl et al. (2020) and Jungclaus et al. (2022), a 20-year average is taken around the doubling of CO_2 in order to reduce the potential influence of internal variability. The TCR is 1.7 K for the 160/40 configuration and 1.6 K for the 80/20 configuration (Fig. 11a,b). The assessment of climate sensitivity in CMIP6 models shows a best estimate of TCR=1.8 K with a very likely range of 1.2 to 2.4 K.

ECS is approximated with the so-called "effective climate sensitivity" (Gregory et al., 2004) using an idealized experiment where the atmospheric CO_2 concentration is abruptly quadrupled (4xCO_2). For this, a linear regression is applied between the global mean surface air temperature change (relative to the CTRL experiment) and the net downward radiative flux at the top-of-atmosphere over 150 years of the simulation (see Fig. 11c,d). The extrapolation of the regression line to zero net radiation gives the temperature response with quadruple increase in CO_2, which is then divided by two to get an estimate for the ECS. This results in an ECS of 2.47 K for the 160/40 configuration and 2.32 K for the 80/20 configuration. The assessment of climate sensitivity in CMIP6 models shows a best estimate of ECS=3 K with a very likely range of 2 to 5 K (Forster et al. 2021). The climate sensitivity of ICON XPP falls within these CMIP6 ranges, tending towards the lower end of the spectrum.

https://doi.org/10.5194/egusphere-2025-2473
Preprint. Discussion started: 12 June 2025

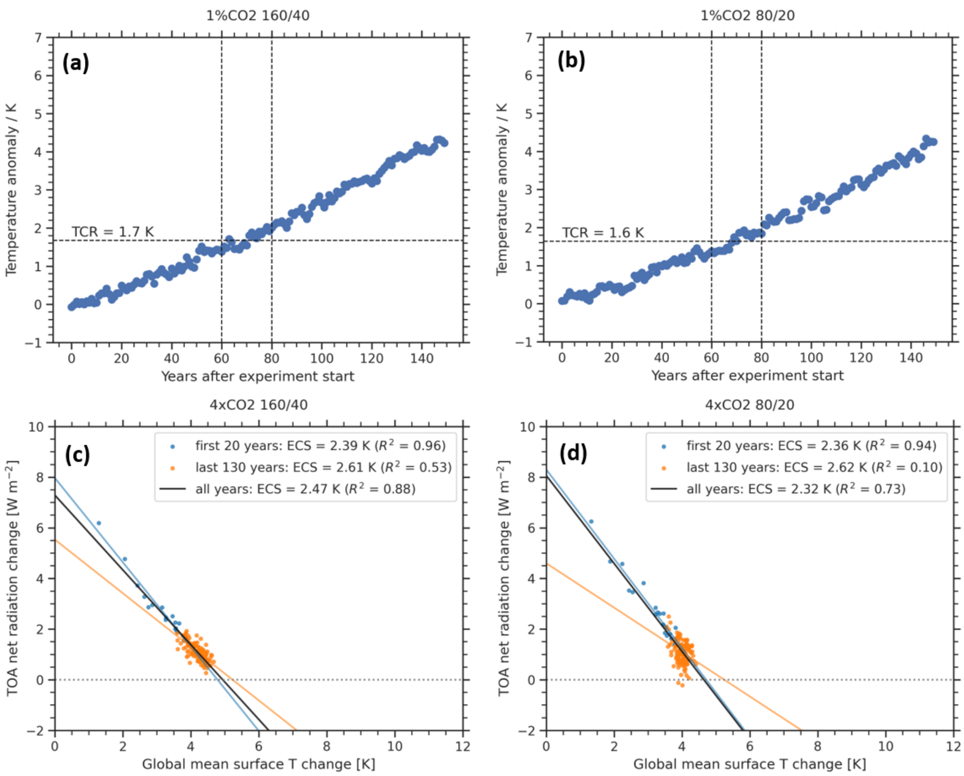

Figure 11: Estimating climate sensitivity. The Transient Climate Response (TCR) is estimated from the global mean surface air temperature anomaly at the time of CO_2 doubling (at year 70) in the 1%CO_2 experiment for (a) 160/40 and (b) 80/20. The Equilibrium Climate Sensitivity (ECS) as diagnosed from scatterplot between TOA net radiance and global mean surface temperature anomaly, including linear regression for (c) 160/40 and (d) 80/20. ECS is estimated from 150 years of the 4xCO_2 experiments (black line), but since the assumption of linear feedback is only an approximation, regression lines and estimated ECS values for the first 20 years (blue line) and the last 130 years (orange line) are shown for completeness.

4. Key dynamical processes in the tropics, extra-tropics and stratosphere

ICON XPP is intended to be the successor of MPI-ESM for climate prediction research and operational forecasts. A principal foundation of climate predictions is based on the reliable description of the principle modes of variability and their associated background mean state. Examples of such modes of variability are the Madden-Julian Oscillation (MJO), ENSO, and the Quasi-Biennial Oscillation (QBO) in the tropics, or the NAO and the extra-tropical jet position in the extra-tropics. While designing the model configurations, we therefore put

https://doi.org/10.5194/egusphere-2025-2473
Preprint. Discussion started: 12 June 2025

special emphasis on monitoring certain aspects of the mean climate which are directly related to the principle modes.

4.1 Tropics

In contrast to the mid-latitudes, the release of latent heat is the main source of energy in the tropics. This occurs in conjunction with convective cloud systems embedded in large-scale circulations. The diabatic heating associated with tropical precipitation not only leads to a localised response in the atmospheric circulation, but can also cause a remote response through the excitation of equatorial waves.

4.1.1 Tropical Waves and Madden-Julian Oscillation

Equatorially trapped waves are a fundamental property of tropical dynamics and appear as solutions of the shallow water equations which are either symmetric or asymmetric about the equator. Among others, the observed disturbances in the clouds can be associated with equatorial trapped waves (Wheeler and Kiladis, 1999). By creating the wavenumber-frequency spectrum of the outgoing longwave radiation (OLR), modes of tropical variability can be analysed in more detail (Wheeler and Kiladis, 1999). The use of OLR implies the assumption that it is a reasonably well-described proxy for deep tropical convection and thus precipitation.

The principal nature of the tropical spectrum is red in both zonal wavenumber and frequency, with highest power at the lowest frequency and lowest zonal wavenumber. Thus, an estimated background spectrum is removed prior to the analysis of tropical waves. Most of the peaks then follow the dispersion curves of equatorial trapped waves, which are also called convectively coupled equatorial waves. However, the MJO and tropical depression-type (TD) disturbances are also present in the spectra. Most of the preferred modes of variability observed in the symmetric component are the MJO (eastward zonal wavenumber 1-5, frequencies of about <= 1/(30 days)), Kelvin waves (eastward zonal wavenumber), Equatorial Rossby waves (ER, westward zonal wavenumber) and westward inertio-gravity modes (WIG, westward zonal wavenumber, frequencies < 3 days). In general, the wavenumber-frequency spectrum has a lower spectral power in the model compared to ERA5 (Fig. 12). However, except for the WIG, the preferred modes of variability in ICON XPP (Fig.12 b,c) match with the observations (Fig. 12a) quite well, with an improvement in the Kelvin waves for the higher resolution 80/20 compared to the 160/40 configuration.

https://doi.org/10.5194/egusphere-2025-2473
Preprint. Discussion started: 12 June 2025

Most of the signals in the antisymmetric component can be associated with Mixed Rossby-Gravity waves (MRG) and Eastward Inertia Gravity waves (EIG) (Fig. 12d). Again, the modes of variability of the antisymmetric component are found in ICON XPP, and improve with higher resolution. One exception is the lack of the strong signal of the n=1 WIG waves (cmp. Fig. 12a and Fig. 12b,c). Both configurations show an improved representation of the equatorial waves compared to ICON-ESM (Jungclaus et al., 2022).

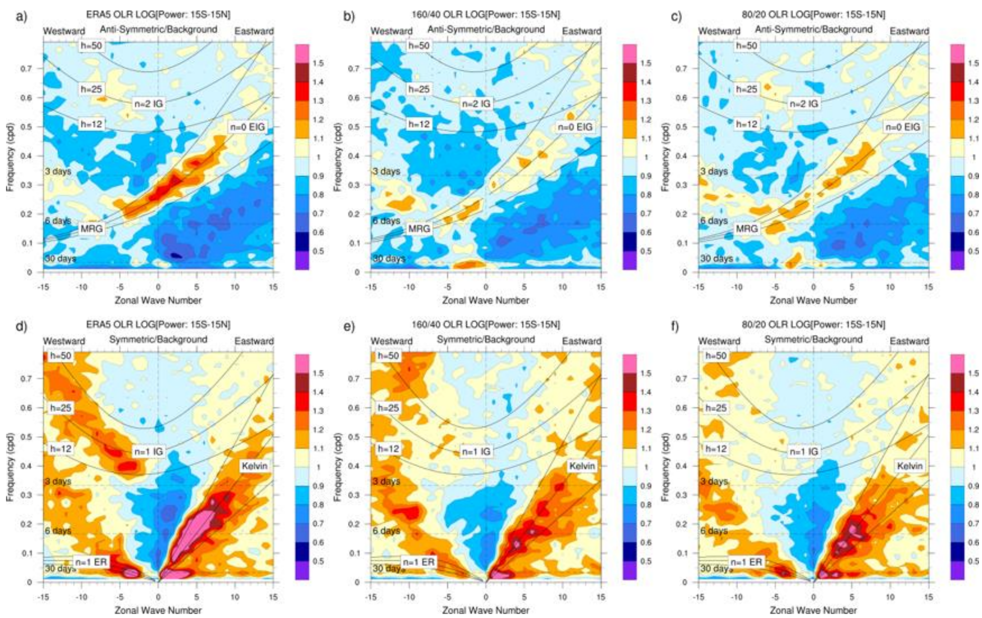

Figure 12: Averaged wavenumber-frequency OLR spectra for the symmetric components (top) and asymmetric components (bottom) between 15° S and 15° N for (a,d) ERA5, (b,e) 160/40 and (c,f) 80/20. Solid lines represent the dispersion curves of the odd (top) and even (bottom) meridional mode-numbered equatorial waves for the three equivalent depths of h = 12, 25, and 50 m [as in Wheeler and Kiladis, 1999]. For ICON XPP, high frequency output of a 10-year period (2000-2010) of one realization is used for both configurations.

4.1.2 El Niño/Southern Oscillation (ENSO)

The El Niño/Southern Oscillation (ENSO) is one of the key processes for climate predictions on seasonal to annual time scales, and is routinely predicted in numerous operational forecast systems. However, ENSO is determined by the complex interplay of the mean climate state in the tropical Pacific, the internal ENSO dynamics (Guilyardi et al., 2020), and also by global

https://doi.org/10.5194/egusphere-2025-2473
Preprint. Discussion started: 12 June 2025

remote influences, for example the Atlantic and Indian Oceans (Cai et al., 2019). In many forecast systems and their underlying Earth system models, the mean state and trends of the tropical Pacific - and thus the ENSO dynamics - are only inadequately represented (Guilyardi et al., 2020). CMIP-like models show long-term mean errors ("cold tongue bias") and strongly underestimated ENSO feedbacks. The MPI-ESM, for example, clearly has weak Bjerknes feedbacks and atmospheric damping in conjunction with a strong tropical Pacific cold bias (Bayr et al., 2019). This has an impact on the simulated development of an ENSO event. A balanced interplay between the mean state and the ENSO dynamics in the tropics can therefore be assumed as a basic prerequisite for successful ENSO predictions.

We investigate ENSO during the tuning process with a particular focus not only on isolated ENSO performance (e.g. amplitude, seasonality etc), but also consider the ENSO dynamics (feedbacks) and the ENSO relation to the mean state bias. We apply the ENSO metric package developed by CLIVAR (Planton et al., 2021), which is designed to evaluate the model with respect to the basic state, ENSO performance and their feedbacks, as well as the ENSO teleconnections. Nino3.4-related SST anomalies for both configurations clearly exhibit an ENSO pattern in the tropical Pacific for both configurations (Fig. 13). The strongest anomalies are found in the central-to eastern Pacific similar to the reference. As many coupled models, ENSO activity in ICON XPP exhibits a stronger westward extension of the SST anomalies than observed (Capotondi et al., 2020).

Figure 14 gives more details of ENSO for the two configurations. Fig. 14a shows a general summary of several metrics from the CLIVAR ENSO package and illustrates ENSO-related mean states, performance, feedbacks and teleconnections in ICON XPP relative to the CMIP6 models. Values within the box indicate that ENSO in ICON XPP is within 90% confidence intervals of the CMIP6 model ensemble. Positive values that are outside the box show that the experiments have a significantly weaker performance than the CMIP6 models. Clearly, for the performance, feedbacks and teleconnection metrics ENSO in ICON XPP is within the range of the CMIP6 models. The ENSO-related mean state summary, however, indicates a larger bias compared to the CMIP6 ensemble. A general improvement is found for all for higher resolution experiments (80/20) compared to the 160/40 runs.

We further examine ENSO by looking into the individual metrics. The mean SST illustrates that the model configurations are about 1.5-2 °C colder than the reference, mainly in the western and central Pacific, associated with the cold-tongue bias (Fig. 14b). The west-east SST

https://doi.org/10.5194/egusphere-2025-2473
Preprint. Discussion started: 12 June 2025

gradient is about 4 °C and is close to what is shown in the Tropflux reference. In the western Pacific the SST gradients are relatively steep in both configurations associated with stronger surface wind stress (Fig. 14c). In the central Pacific the SST gradient flattens in both configurations and the surface wind stress becomes smaller than observations. The higher-resolved configuration substantially improves the ENSO-related wind stress, while in the 160/40 resolution the maximum surface wind stress is much stronger and shifted too far westward. In addition, we show the zonal mean total precipitation for the Pacific (Fig. 14d). The distributions clearly reveal a double-ITCZ in both configurations, with a strong deviation from observations shown in the Southern Pacific. The bias is relatively large in both configurations with values up to 4-5 mm/day. The double ITCZ bias is found in many coupled models, and is linked with their ENSO characteristics, such as ENSO seasonal phase-locking simulation (Liao et al., 2023).

The ENSO characteristics of the two configurations are shown in Figure 14e-g. The ENSO amplitude across the tropical Pacific shows weaker values in the eastern part and stronger values in the western part (Fig. 14e) associated with mean state wind stress distribution (Fig. 14c). The amplitude of the Nino3.4 index appears a bit weak and is about 2/3 of the observational amplitude. During the peak season of ENSO the Nino3.4 index is about 0.7 and 0.8°C in 160/40 and 80/20 compared to 1.2 °C in Tropflux (Fig. 14f). In addition, the ENSO skewness shows larger (smaller) values in the western (eastern) Pacific and indicates a western shift of the peak ENSO (Fig. 14g).

Finally, we show the ENSO feedbacks, since they characterize the dynamical evolution of ENSO (Fig. 14h-j). A positive wind stress-SST relationship explains an anomalous zonal wind with the SST propagation along the tropical Pacific. For example, during El Niño, a stronger wind stress (weaker trade winds) is associated with eastward propagation of SST anomalies. This relationship is captured in both configurations, but with less amplitude and the maximum regression coefficients appear shifted eastward compared to observations (Fig. 14h). The wind stress is furthermore related to thermocline depth, meaning that for example during El Niño there is a shallowing (deepending) of the thermocline depth in the western (central-to-eastern) Pacific (Fig. 14i, here the thermocline depth is illustrated by the sea surface height SSH). In both configurations, the negative wind stress-SSH relationship in the western Pacific is absent, while positive regression coefficients are found in the central-to-eastern Pacific. In the central-to-eastern Pacific, the 80/20 configuration shows regression coefficients relatively close to

https://doi.org/10.5194/egusphere-2025-2473
Preprint. Discussion started: 12 June 2025

observation. Finally, the negative SST-heat flux relationship illustrates the atmospheric damping effect, i.e. in case of El Niño, a warm SST anomaly results in a stronger updraft and cloud cover increase which in turn reduces the net incoming radiation at the surface (Fig. 14j). In ICON XPP this feedback is strongly underestimated which reflects a systematic bias in the heat fluxes, in particular in the central-to-western Pacific. This is a common bias found in many CMIP models, in which a weak atmospheric heat flux damping compensates the weak Bjerknes feedback (Bayr et al., 2019). The weak SST-heat flux relationship in ICON XPP is dominated by the shortwave radiation fluxes (not shown), similar to what is found in other models (Bayr et al., 2019).

In summary, ICON XPP generates an ENSO with typical characteristics and dynamics known from observations. However, with the current parameter setting ICON XPP performs weaker amplitudes and feedbacks compared to observations, but a significant improvement is found for 80/20 compared to 160/40. We also find structural biases similar to the long-standing errors of many coupled models. Here, the overall performance with respect to the CMIP6 models reveal pronounced biases in both configurations, closely associated with the precipitation bias. However, in other key diagnostics - performance, feedbacks and teleconnections - ENSO in ICON XPP is within the range of the CMIP6 models.

It is worth noting that in some aspects both configurations share similar features. An example is the precipitation bias which clearly indicates a pronounced double-ITCZ, or the weak ENSO amplitudes in both configurations. This points towards systematic errors covered in both configurations. Given that the 160/40 configuration is much faster and cheaper than 80/20, this poses an opportunity to test and eventually improve the ENSO fidelity by the examination of a much broader parameters space in 160/40, than it would be possible in 80/20. First attempts point towards the role of cloud properties and microphysics in modulating the surface radiation budget and have an effect on the atmospheric damping and the SST- wind stress feedbacks. This work is in progress.

https://doi.org/10.5194/egusphere-2025-2473
Preprint. Discussion started: 12 June 2025

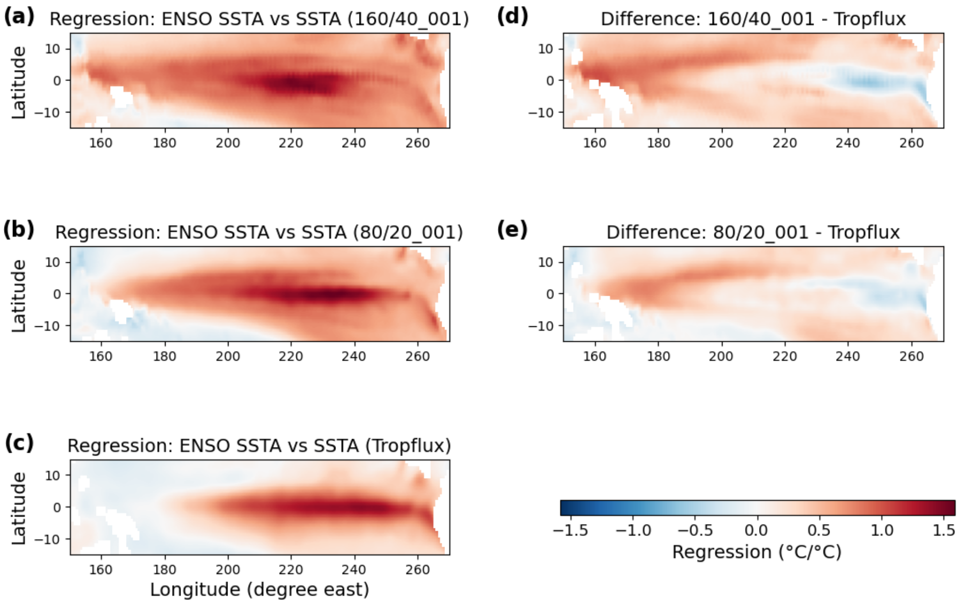

Figure 13: Regression between Nino3.4 index and SST anomalies (SSTA) for December for one member of (a) 160/40, (b) 80/20, and (c) and TropFlux. Also shown are the differences between (d) 160/40 and TropFlux, and (e) 80/20 and TropFlux. Units are in [°C/°C]. The regression is calculated with the CLIVAR ENSO metric package (see Planton et al. (2021) for details).

https://doi.org/10.5194/egusphere-2025-2473
Preprint. Discussion started: 12 June 2025

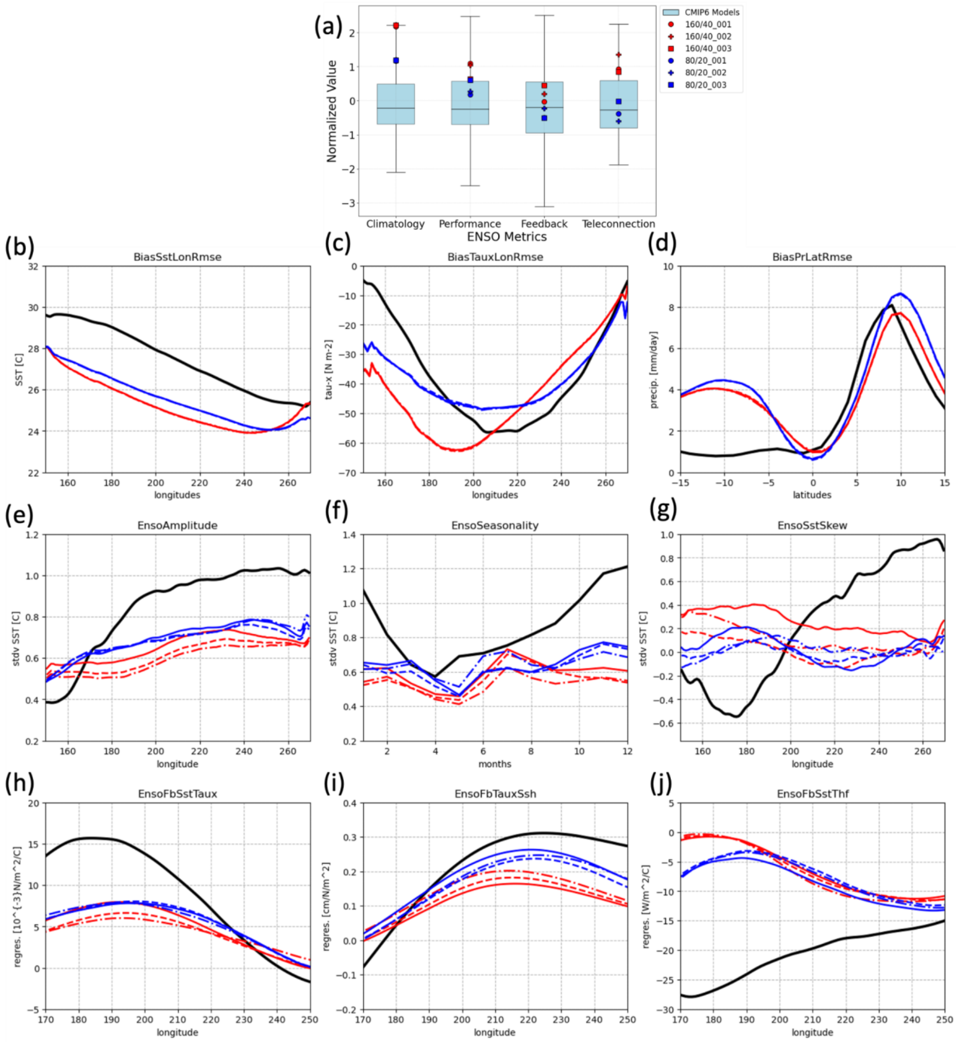

Figure 14: Description of ENSO. (a) An overall summary of different categories of the ENSO metrics (climatology, characteristics, feedbacks and teleconnections) for (red) the 160/40 and (blue) 80/20 ensemble members together with the CMIP6 models. See Planton et al. (2021) for all metrics and their definitions. Further shown are specific metrics for (b-e) ENSO-related climatology, (e-g) ENSO characteristics, and (h-j) ENSO feedbacks for (red) the 160/40 and (blue) 80/20 configurations, and (black) an observational reference. The mean states are illustrated by (b) SST averaged for 5° N to 5° S, (c) the zonal wind stress averaged for 5° N to 5° S, and (d) the precipitation averaged for 150° W to 90° W. The ENSO characteristics are described by (e) the zonal structure of the standard deviation of the Nino3.4 SST anomalies (SSTA) averaged for 5° N to 5° S, (f) the standard deviation of SSTA as a function of calendar months, (g) the skewness of SSTA in the equatorial Pacific averaged for 5° N to 5° S. ENSO is further analysed by the Bjerknes feedbacks, here shown by (h) the regression of zonal wind-stress anomalies (meridional 5° S to 5° N average) onto SSTA in the eastern equatorial Pacific (Niño3 region

https://doi.org/10.5194/egusphere-2025-2473
Preprint. Discussion started: 12 June 2025

averaged), and (i) the regression of sea-surface height (SSH) anomalies (meridional 5° S to 5° N average) on to wind-stress anomalies (Niño3 region averaged). The atmospheric damping is illustrated by (j) the regression total atmospheric surface heat flux anomalies on SSTA, both 5° N to 5° S averaged. The plots are calculated based on the CLIVAR ENSO metric package (Planton et al., 2021). As references this package uses GPCPv2.3 for precipitation, AVISO for SSH, and Tropflux otherwise (Praveen Kumar et al., 2012).

4.2 Extra-tropics - Zonal mean zonal wind and jets

The extra-tropical jets provide a substantial guideline for synoptic-scale disturbances. Among other, the extra-tropical storm paths are aligned to the position and magnitude of the seasonally and yearly varying jet positions and impact weather and climate further downstream. In addition, the time-averaged tropospheric jets act as a wave-guide for Rossby-like traveling waves propagating from the tropical regions to the extra-topics, and thereby have a control on the mid-latitude dynamics (Branstator 2002). In the extra-tropics, the zonal and meridional jet variation mark a fundamental property of the major modes of climate variability, i.e. NAO (Woolings et al., 2015), and its predictability (i.e. Strommen et al., 2023). The NAO constitutes a principal driver of the North Atlantic and European climate, and meanwhile seasonal and decadal prediction skill is established in various prediction systems and underlying coupled models (Doblas-Reyes et al., 2003, Müller et al., 2005, Scaife et al., 2014, Dobrynin et al., 2018, Smith et al., 2020, Athanasiadis et al., 2020).

However, climate models still provide biases in the representation of the zonal wind, and associated jets and storm tracks. For example, CMIP6 models are generally able to reproduce storm tracks, however, they appear too zonal over the Pacific and Atlantic (Priestly et al., 2020). Over the southern hemisphere, the models tend to shift jet positions and storm tracks too far equatorwards. There is a general improvement in the biases from CMIP5 to CMIP6, which arises from the tendency of using higher model resolutions, but their bias structures still persist (Priestly et al., 2023). In MPI-ESM used for CMIP6, the mean zonal wind and storm track biases are reduced by doubling the atmospheric resolutions. The bias reduction is mainly induced by an improved wave-activity flux and eddy-driven effects on the mean zonal wind, particularly of the Northern hemisphere jet exits (Müller et al., 2018). However, a relatively strong zonal wind bias persists in the higher-resolved model version. In this respect, the underestimation of eddy-driven effects on the mean zonal wind is found in many climate models (i.e. Smith et al., 2022).

https://doi.org/10.5194/egusphere-2025-2473
Preprint. Discussion started: 12 June 2025

In ICON XPP, the zonal mean zonal wind biases in the extra-tropics appear smaller compared to its predecessors ICON-ESM (Jungclaus et al., 2022) and MPI-ESM (Müller et al., 2018) In the 80/20 configuration, a bias of 1-2 m/s is found at the northern hemisphere jet position (Fig. 15), and of 2-4 m/s in the low resolution (160/40). For comparison in MPI-ESM, zonal mean zonal wind biases are about twice as large and amount to 2-4 m/s and >4 m/s for similar resolutions compared to ICON XPP (cf Fig. 9 in Müller et al., 2018). For ICON-ESM, a bias of up to 10 m/s is found in their 160/40 configuration (cf Fig. 12 in Jungclaus et al., 2022). In the tropics, there are alternating significant positive and negative biases varying with height. The biases are smaller compared to ICON-ESM but of similar magnitude compared to MPI-ESM.

To understand the reasons for the relatively small biases of the northern hemisphere zonal winds, we further examine the eddy-mediated effects on the jets. Figure 16 shows the mean zonal wind at a level where the jet maximum occurs and corresponding divergence of 2-6 day bandpass-filtered eddy-momentum fluxes. The divergence is calculated based on the horizontal components of the E-vector averaged over 200-300 hPa (Hoskins et al., 1983). The net effect of the divergence is a westerly acceleration, whereas a convergence is associated with increased easterlies. ERA5 reveals maximum divergence at the jet exits indicative for jet extension by eddy-momentum fluxes. The figure further shows that momentum fluxes are able to force the jets towards the north-eastward direction. In ICON XPP, eddy-momentum fluxes are found similar to ERA5 and the jet is forced towards a north-eastward direction. That is different to precursors of ICON XPP, where momentum fluxes and respective jets appear more zonally oriented. The magnitudes of the divergence of the momentum fluxes in 160/40 are higher than in ERA5, but fits very well in 80/20. This diagnostic underlines the well-behavior of the synoptic properties in ICON XPP for the mean state of the jet. It can be expected that this has a positive impact on storm-track pathways and associated impact on downstream regional climate.

https://doi.org/10.5194/egusphere-2025-2473
Preprint. Discussion started: 12 June 2025

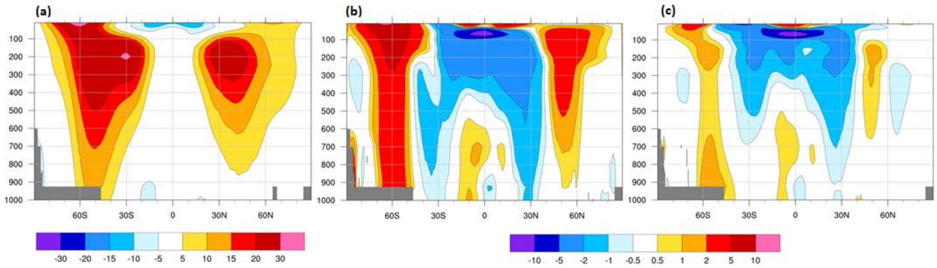

Figure 15: (a) Annual man zonal mean zonal wind in the troposphere for the period 1979-2008 for ERA5 and biases for the (b) 160/40 and (c) 80/20 resolutions. Units are [m s^{-1}].

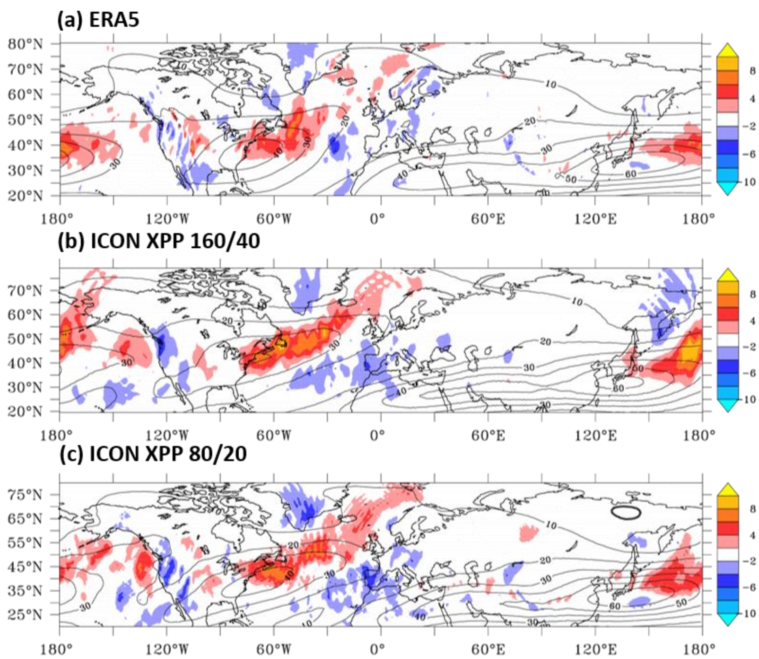

Figure 16: The effect of transient eddies on the mean state. Shown is the divergence of the E-Vector (shading) and the mean zonal wind (contours), for winter means (DJF) in (a) ERA5 (period 2000-2010) and 10-year averages for the ICON XPP (b) 160/40 and (c) 80/20 resolutions. The E-Vector is calculated by $\nabla(u^2 + v^2, -uv)$, where u and v are 2-6 day band-pass filtered zonal and meridional wind anomalies. The E-vector and mean zonal wind are averaged between 200-300 hPa. Positive values of the divergence indicate a transfer of momentum to the mean state.

4.3 Stratosphere - QBO, Polar Vortex and Sudden Stratospheric Warmings

https://doi.org/10.5194/egusphere-2025-2473
Preprint. Discussion started: 12 June 2025

Developments in recent decades have shown that seasonal and long-range climate predictions benefit from resolving the stratosphere at depth, as the variability of the stratosphere is not only affected by the lower atmosphere and surface climate, but also by intrinsic interactions (e.g. Manzini et al., 2014, Domeisen et al., 2020 a,b, Scaife et al., 2022). The quasi-biennial oscillation (QBO), the polar vortex variability, and associated major sudden stratospheric warmings (MSSW) are key processes in this respect.

The QBO is an important component of the Earth's climate, controlling equatorial zonal winds and temperature deviations from the global mean. Its teleconnections to surface climate occur in various pathways (Gray et al., 2018). In the tropics, a link between the tropical stratosphere and the MJO has been revealed as the phase of the QBO modulates the MJO (e.g. Martin et al., 2021). In addition, the QBO modulates the winter stratospheric polar vortex in the Northern Hemisphere, which has implications for the troposphere (Holton and Tan, 1982). Both the QBO and the variability of the stratospheric polar vortex are examples of predictability originating in the stratosphere.

The observed QBO is characterized by descending alternating easterly and westerly jets in the tropical stratosphere, shown by the zonally averaged zonal wind (Fig. 17a). These jets are even more pronounced in the wind anomalies, shown as deviations from the long-term average (Fig. 17d). In the ICON XPP 160/40 configuration, with 90 vertical levels, the descending winds are weak easterly winds with a high periodicity compared to observations (Fig. 17b). For the higher resolution 80/20 with an increased number of vertical levels, a QBO is present, although the amplitudes still appear smaller than observations, and the frequency is still higher than observed (Fig. 17c,f). The zonal wind anomalies emphasize that ICON XPP is capable of developing spontaneous QBO phases (Fig. 17e,f). However, in 160/20 with 90 vertical levels, the QBO is more disruptive and not well established (Fig. 17e). In agreement with previous findings, an increase of the number of vertical levels improves the representation of the QBO (Fig. 17e,f). The long-term mean equatorial zonal mean wind is characterized by strong easterly winds, which can be seen in the resulting profile at about 20 km height in the historical simulations of ICON XPP. These easterly winds can act as a permanent wave filter for vertical wave propagation, resulting in a perturbed wave forcing above that height, hindering the QBO development in ICON. The reason for the development of this easterly jet is unclear, but seems to be connected on the horizontal resolution.

https://doi.org/10.5194/egusphere-2025-2473
Preprint. Discussion started: 12 June 2025

In atmosphere-only experiments (160 km, 130 level), the frequency of the QBO phases is improved Niemeier et al. (2024). In their experiments the QBO is well established. In addition, the stratospheric transport is well represented, and, consequently, the transport of the water vapour cloud after the Honga Tonga eruption is very close to observations. These changes have not yet been applied to the presented coupled configurations.

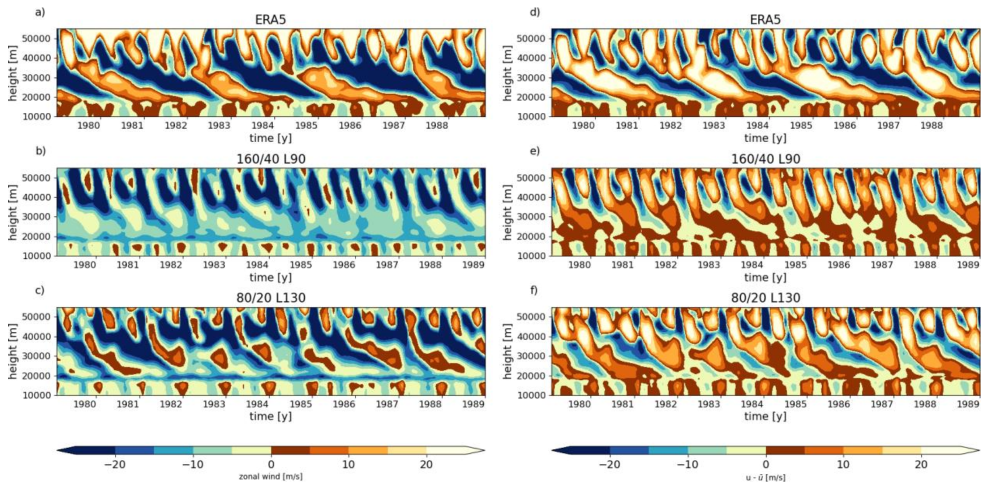

Figure 17: Zonal mean zonal wind averaged between 5° S and 5° N in a) ERA5, b) 160/40 with 90 vertical levels (L90) and c) 80/20 with 130 vertical levels (L130) and d), e), f) the corresponding deviation of the long-term mean (1979-2008). Here the period 1979-1989 is shown. Units are in [m s^{-1}].

In the extra-tropics, the northern hemispheric stratospheric polar vortex is a key element of the troposphere-stratosphere system. However, several factors - among others volcanic eruptions, ENSO events, the MJO and the 11-year solar cycle - influence the upward propagation of large-scale Rossby waves from the troposphere that affect the variability of the polar vortex, and make their complete description difficult. The tropospheric circulation in turn changes after weak stratospheric vortex events - namely major sudden stratospheric warmings (MSSW). An MSSW event, defined as reversal of the zonal mean zonal wind from westerlies to easterlies at 60°N at 10 hPa accompanied by a polar stratospheric temperature increase, is usually followed by a weakening and a shift in the mid-latitude tropospheric jet (Scaife et al., 2022 and references therein). These changes have a similar time scale to the changes in the lower stratosphere and thus enable an extension of the predictability beyond the deterministic limit of weather forecasts.

https://doi.org/10.5194/egusphere-2025-2473
Preprint. Discussion started: 12 June 2025

The variability of the winter northern hemispheric stratospheric polar vortex shows for example at least 8 major sudden stratospheric warmings during 2000 and 2010 in ERA5 (Fig. 18a). This period, in which the high-frequency output is available, is characterised by an increased occurrence of MSSW events, compared to 5 to 6 events in previous decades. Both the 160/40 and 80/20 configurations exhibit a similar number of stratospheric warmings as ERA5 (Fig. 18b, c). Although 80/20 is not explicitly tuned for the stratosphere, the time series indicate that the northern hemispheric polar vortex exhibits comparable variations as in observations. Further analyses like the differentiation between vortex split and displacement events, the seasonal cycle, the correlation of the eddy heat fluxes at 100 hPa with the vortex variability and the temperature anomaly, or the surface impact are necessary in order to compare the dynamics of the generated MSSW frequency in ICON XPP with observations (e.g. Charlton et al., 2007).

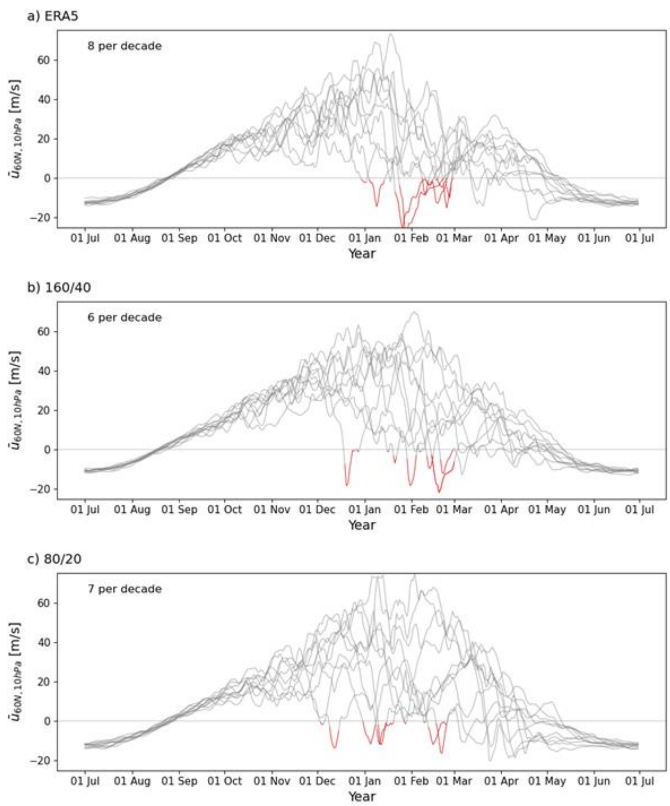

https://doi.org/10.5194/egusphere-2025-2473
Preprint. Discussion started: 12 June 2025

Figure 18: Daily zonal mean zonal wind at 60° N, 10 hPa for a) ERA5, b) 160/40 and c) 80/20. For b) and c) high-frequency output is used. Here, the period 2000/2001-2009/2010 is used for ERA5 and ICON XPP. Units are [m s^{-1}].

5. Discussion and Conclusion

ICON XPP is a newly developed Earth System model configuration based on the ICON modeling framework. It merges accomplishments from the recent operational numerical weather prediction model (ICON NWP) with well-established climate components for the ocean, land and ocean-biogeochemistry into a new Earth System model configuration. Here, we discussed two baseline configurations which serve as a starting point for accommodating ICON for Earth System predictions and projections, and future model development.

ICON XPP in the presented configurations reaches typical targets of a coupled climate simulation, such as a pre-industrial stable climate equilibrium with radiation balance and a target global mean temperature. Though the presented configurations share some long-standing biases in coupled models, such as the warm biases in the coastal upwelling regions, the overall fidelity of ICON XPP fits in the CMIP6 ensemble, as diagnosed by a few key parameters. This is noteworthy since a major newly implemented component is the atmospheric model component ICON NWP, originally designed for numerical weather prediction, which is tested here for the first time in a coupled Earth System configuration. Furthermore, the climate sensitivity, albeit weak, fits within the assessed range of the CMIP6 models, and creates confidence in ICON XPP projections. The simulated trends of global temperature, close to observations, underline the model's suitability to simulate various climate scenarios.

The model configurations are able to capture the principal features of coupled circulations in the tropics. A prominent example is ENSO, which reveals typical characteristics and dynamics known from observations, in both configurations. We highlighted the use of a more sophisticated evaluation of ENSO, by not only looking at certain characteristics (amplitude, spectra, skewness etc.), but also considering the ENSO dynamics (feedbacks) and its link to the mean bias. Although ENSO amplitudes and basic feedbacks appear weak, the overall fidelity of ENSO in ICON XPP fits within the CMIP6 models. Further examples of key processes in the tropics are the tropical waves and Madden-Julian Oscillation, which - analyzed by the wavenumber-frequency analysis - are captured quite well in both configurations. In addition, ICON XPP is capable of developing spontaneous QBO phases, which clearly benefits from the higher vertical resolution in the 80/20 configuration.

https://doi.org/10.5194/egusphere-2025-2473
Preprint. Discussion started: 12 June 2025

An outstanding result of the current evaluation is the state of the northern-hemisphere extra-tropical dynamics. Here, ICON XPP reveals a strong reduction of the tropospheric zonal mean zonal wind biases, and the location of the mean jets are placed close to what is found in observations. A closer examination of the synoptic-scale eddies reveals that ICON XPP is able to depict the shape and magnitude of the transfer of momentum onto the mean flow close to what is found in ERA5. The momentum transfer leads to a northeastward elongation of the mean jet in ICON XPP, whereas predecessor model generations reveal a strong zonal distribution. This could have consequences for the storm tracks and their downstream impacts, which are known to exhibit a biased southern pathway in the ICON XPP precursors. We hypothesize that this improvement is linked to the enhanced accuracy in resolving synoptic disturbances within the ICON NWP model.

However, the current configurations are characterized by some strong biases with global implications. These include a warm bias of up to 5°C in the Southern Ocean, associated with little sea-ice. Accompanied with this are a particularly deep ocean mixed layer at the Antarctic boundaries near the Weddell Sea and strong biases in the atmospheric net radiation and cloud covers (not shown). Errors of this magnitude inevitably lead to the need to adjust the model. In order to achieve the global mean temperature target, it was necessary to counterbalance the Southern Ocean warming by adjustment of cloud parameters, e.g. reducing the entrainment rate. Further, the Southern Ocean plays an important role in remote regions of the climate system. Recent studies reveal the global role of the observed Southern Ocean cooling trends and their teleconnections, such as to tropical regions and the southeast Pacific cooling (Kang et al., 2023). However, many climate models notoriously fail to capture the recent SST trend in the Southern Ocean. Also, all coupled model and climate prediction systems are not able to capture the Pacific cooling trend with consequences on forecasting the Pacific climate such as ENSO (e.g. l'Heureux et al., 2022). Therefore, an improvement of the Southern Ocean climate may be of great relevance for remote regional climate and their predictions.

The tropical precipitation distribution reveals the long-standing double ITCZ, as found in many CMIP6-like models. In our configurations, however, the magnitudes are relatively large compared to the CMIP6 ensemble. Such a bias ultimately imposes an influence on regional and global climate. An example is ENSO, which provides a strong relationship to the precipitation bias in the current ICON XPP configuration. Further, a strong dry bias in the Amazonian region is found in the current configurations. Such bias imposes an impact on the modeling of land

https://doi.org/10.5194/egusphere-2025-2473
Preprint. Discussion started: 12 June 2025

vegetation and the global carbon cycle. The reasons for the tropical precipitation bias are yet unclear. However, since during the tuning process the precipitation distribution has not received much attention, we expect some improvements in subsequent versions of ICON XPP.

ICON XPP forms the basis for future developments in the areas of climate predictions and projections. Some initiatives have already been established for this purpose. One project was initiated to support ICON XPP's preliminary research into climate predictions. Here, data assimilation methods and hindcasts are being tested with ICON XPP, as well as their possibilities for special applications. The aim is, among others, to use ICON XPP for operational climate predictions. Another initiative prepares ICON XPP as a national contribution to CMIP7. For this, ICON XPP will be more thoroughly tuned with respect to the aforementioned biases. In addition, corresponding DECK experiments with CMIP7 forcing will be prepared and carried out, and their data disseminated. A basic requirement for both initiatives is that the model is able to calculate as many model years and ensemble members as possible, in as little real time as possible. The high runtime performance of the current configurations with throughput of ~80 simulated years per day (SYPD, 100 nodes) for 160/40 and ~45 SYPD (64 nodes) for 80/20 - run on a CPU-partition of the DKRZ HPC - meet this requirement.

In summary, ICON XPP is an Earth System model configuration, able to run long integrations and large-ensemble experiments, making it suitable for climate predictions and projections, and for climate research for which a large throughput is required.

Acknowledgments

We would like to acknowledge the German Climate Computing Center (DKRZ) for providing the computing facilities used to run the simulations. This research was supported by the German Ministry of Education and Research (BMBF) by the project Coming Decade (WM, DY - grant 01LP2327E) and CAP7 (MS - grant 01LP2401C). AS received funding from DWD’s “Innovation Programme for Applied Researches and Developments” IAFE ICON-Seamless VH 4.7. CAK received funding from the ETH Postdoctoral Fellowship programme, her model tuning work/GPU port testing was supported by a grant from the Swiss National Supercomputing Center (CSCS) under the project ID s1283 on Alps. HP has received funding from the European Union’s Horizon Europe research and innovation programme under grant agreement No 101081460. Views and opinions expressed are, however, those of the author(s)

https://doi.org/10.5194/egusphere-2025-2473
Preprint. Discussion started: 12 June 2025

only and do not necessarily reflect those of the European Union. Neither the European Union nor the granting authority can be held responsible for them. UN received support from the Deutsche Forschungsgemeinschaft (DFG) Research Unit VolImpact (FOR2820, grant no. 398006378) within the project VolARC and simulations on stratosphere and QBO tuning have been performed at DKRZ using resources granted by its Scientific Steering Committee (WLA, under project ID bm0550). We thank Marco Giorgetta for reviewing the manuscript before submission.

Code and Data Availability Statement

The run scripts and manual used to run ICON XPP for this study are available in the Open Research Data Repository of the Max Planck Society (https://doi.org/10.17617/3.UUIIZ8) (Müller et al., 2025). ICON is available to the community under a permissive open source licence (BSD-3C). Please follow the instructions on the ICON web-page (https://www.icon-model.org/). ERA5 data (Hersbach et al., 2020) was downloaded from the Copernicus Climate Change Service (2019a, 2019b). The results contain modified Copernicus Climate Change Service information 2025. Neither the European Commission nor ECMWF is responsible for any use that may be made of the Copernicus information or data it contains. Figures 6a, 6b, 7, and 8 of this study have been created with the Earth System model Evaluation Tool (ESMValTool; Righi et al., 2020; Andela et al., 2024a) and its core dependency ESMValCore (Andela et al., 2024b). ESMValTool has recently been extended to be able to process ICON XPP output without any model postprocessing (Schlund et al., 2023). CMIP6 model output required to reproduce the analyses of this paper is available through the Earth System Grid Foundation (ESGF; https://esgf-metagrid.cloud.dkrz.de/search/cmip6-dkrz/, last access: 19 February 2025). ESMValTool can automatically download these data if requested (see https://docs.esmvaltool.org/projects/ESMValCore/en/v2.11.1/quickstart/configure.html#esgf-configuration, last access: 19 February 2025). Observational/reanalysis datasets are not distributed with ESMValTool that is restricted to the code as open source software, but ESMValTool provides a collection of scripts with downloading and processing instructions to recreate all observational/reanalysis datasets used for Figures 6a, 6b, and 7 (see https://docs.esmvaltool.org/en/latest/input.html#observations, last access: 19 February 2025).

Authors Contribution

https://doi.org/10.5194/egusphere-2025-2473
Preprint. Discussion started: 12 June 2025

Conceptualization: WM, TvP, AS, SL. Writing - original draft: WM, TvP, AS, SL, FC. Visualization: TvP, AS, SL, MS, DY, RB, TS. Model component development: VB, NB, FC, KF, VG, HH. SH, MH, TI, JJ, MK, PK, LK, CK, JK, KCM, UN, HP, IP, TR, TS, RW. Supervision: JM, RP, BF.

Competing Interests

The contact author has declared that none of the authors has any competing interests.

REFERENCES

Adcroft, A., and Campin, J.-M.: Rescaled height coordinates for accurate representation of free-surface flows in ocean circulation models. *Ocean Modelling*, 7(3-4), 269-284, 2004.

Adler, R., Wang, J.-J., Sapiano, M., Huffman, G., Chiu, L., Xie, P.-P., Ferraro, R., Schneider, U., Becker, A., Bolvin, D., Nelkin, E., Gu, G., and NOAA CDR Program: Global Precipitation Climatology Project (GPCP) Climate Data Record (CDR), Version 2.3 (Monthly), https://doi.org/10.7289/V56971M6, 2017.

Andela, B., Broetz, B., de Mora, L., Drost, N., Eyring, V., Koldunov, N., Lauer, A., Mueller, B., Predoi, V., Righi, M., Schlund, M., Vegas-Regidor, J., Zimmermann, K., Adeniyi, K., Arnone, E., Bellprat, O., Berg, P., Bock, L., Bodas-Salcedo, A., Caron, L.-P., Carvalhais, N., Cionni, I., Cortesi, N., Corti, S., Crezee, B., Davin, E. L., Davini, P., Deser, C., Diblen, F., Docquier, D., Dreyer, L., Ehbrecht, C., Earnshaw, P., Gier, B., Gonzalez-Reviriego, N., Goodman, P., Hagemann, S., Hardacre, C., von Hardenberg, J., Hassler, B., Heuer, H., Hunter, A., Kadow, C., Kindermann, S., Koirala, S., Kuehbacher, B., Lledó, L., Lejeune, Q., Lembo, V., Little, B., Loosveldt-Tomas, S., Lorenz, R., Lovato, T., Lucarini, V., Massonnet, F., Mohr, C. W., Amarjiit, P., Pérez-Zanón, N., Phillips, A., Russell, J., Sandstad, M., Sellar, A., Senftleben, D., Serva, F., Sillmann, J., Stacke, T., Swaminathan, R., Torralba, V., Weigel, K., Sarauer, E., Roberts, C., Kalverla, P., Alidoost, S., Verhoeven, S., Vreede, B., Smeets, S.,

https://doi.org/10.5194/egusphere-2025-2473
Preprint. Discussion started: 12 June 2025

Soares Siqueira, A., Kazeroni, R., Potter, J., Winterstein, F., Beucher, R., Kraft, J., Ruhe, L., Bonnet, P., and Munday, G.: ESMValTool, tps://doi.org/10.5281/zenodo.3401363, 2024a.

Andela, B., Broetz, B., de Mora, L., Drost, N., Eyring, V., Koldunov, N., Lauer, A., Predoi, V., Righi, M., Schlund, M., Vegas-Regidor, J., Zimmermann, K., Bock, L., Diblen, F., Dreyer, L., Earnshaw, P., Hassler, B., Little, B., Loosveldt-Tomas, S., Smeets, S., Camphuijsen, J., Gier, B. K., Weigel, K., Hauser, M., Kalverla, P., Galytska, E., Cos-Espuña, P., Pelupessy, I., Koirala, S., Stacke, T., Alidoost, S., Jury, M., Sénési, S., Crocker, T., Vreede, B., Soares Siqueira, A., Kazeroni, R., Hohn, D., Bauer, J., Beucher, R., Benke, J., Martin-Martinez, E., and Cammarano, D.: ESMValCore, https://doi.org/10.5281/zenodo.3387139, 2024b.

Athanasiadis, P. J., Yeager, S., Kwon, Y. O, Belucci, A., Smith, D. W.. and Tibaldi, S.: Decadal predictability of North Atlantic blocking and the NAO. npj Clim Atmos Sci, 3, 20, doi:10.1038/s41612-020-0120-6, 2020.

Bayr, T., Latif, M., Dommenget, D., Wengel, C., J. Harlaß, and Park, W.: Mean-state dependence of ENSO atmospheric feedbacks in climate models. Clim Dyn 50, 3171–3194, https://doi.org/10.1007/s00382-017-3799-2, 2018.

Beobide-Arsuaga, G., Düsterhus, A., Müller, W. A., Barnes, E. A., and Baehr, J.: Spring regional sea surface temperatures as a precursor of European summer heatwaves, Geophysical Research Letters, 50, e2022GL100727, https://doi.org/10.1029/2022GL100727, 2023.

Borchert, L. F., Pohlmann, H., Baehr, J., Neddermann, N.-C., Suarez-Gutierrez, L., and Müller, W. A.: Decadal predictions of the probability of occurrence for warm summer temperature extremes. Geophys. Res. Lett., 46, 14042-14051, doi:10.1029/2019GL08538546, 2019.

Branstator, G.: Circumglobal Teleconnections, the Jet Stream Waveguide, and the North Atlantic Oscillation. *J. Climate*, **15**, 1893–1910, https://doi.org/10.1175/1520-0442(2002)015<1893:CTTJSW>2.0.CO;2, 2002.

Canadell, J.G., et al.: Global Carbon and other Biogeochemical Cycles and Feedbacks. In Climate Change 2021: The Physical Science Basis. Contribution of Working Group I to the Sixth Assessment Report of the Intergovernmental Panel on Climate Change, pp. 673–816, doi:10.1017/9781009157896.007, 2021.

https://doi.org/10.5194/egusphere-2025-2473
Preprint. Discussion started: 12 June 2025

Capotondi, A., Deser, C., Phillips, A. S., Okumura, Y., & Larson, S. M: ENSO and Pacific decadal variability in the Community Earth System model version 2. Journal of Advances in Modeling Earth Systems, 12(12), doi:10.1029/2019MS002022, 2020.

Cai, W. J., Wu, L., Lengaigne, M., Li, T., McGregor, S., Kug, J. S., Yu, J., Stuecker. M. F., Santoso, A.,, Li, X., Ham, Y.-G., Chikamoto, Y., Ng, B., McPhaden, M. J., Du,Y., Dommenget, D., Jia, F., Kajtar, J. B., Keenlyside, N., Lin,X., Luo, J.-J., Martín-Rey, M., Ruprich-Robert, Y., Wang, G., Xie, S.-P., Yang, Y., Kang, S. M., Choi, J.-Y., Gan, B., Kim, G.-I., Kim, C.-E., Kim, S., Kim, J.-H., and Chang, P.: Pantropical climate interactions. Science, 363 (6430), 944-+, doi:10.1126/science.aav4236, 2019.

Charlton, A.J., L. M., Polvani, J.. Perlwitz, F., Sassi, E., Manzini, K., Shibata, S., Pawson, J. E., Nielsen, and D., Rind: A new look at stratospheric sudden warmings. Part II: Evaluation of numerical model simulations. J. Climate, **10**, 470-488, doi:10.1175/JCLI3994.1, 2007.

Copernicus Climate Change Service: ERA5 monthly averaged data on pressure levels from 1940 to present, https://doi.org/10.24381/CDS.6860A573, 2019a.

Copernicus Climate Change Service: ERA5 monthly averaged data on single levels from 1940 to present, https://doi.org/10.24381/CDS.F17050D7, 2019b.

Doblas-Reyes, F. J., Pavan, V. and Stephenson, D.B.: The skill of multi-model seasonal forecasts of the North Atlantic Oscillation. Climate Dyn., 21, 501-514, 2003.

Dobrynin, M., Domeisen, D. I., Müller, W. A., Bell, L., Brune, S., Bunzel, F., Düsterhus, A., Fröhlich K. Pohlmann, H. and Baehr, J.: Improved teleconnection-based dynamical seasonal predictions of boreal winter. Geophysical Research Letters, 45(8), 3605–3614, https://doi.org/10.1002/2018GL077209, 2018.

Dobrynin, M., Düsterhus, A., Fröhlich, K., Athanasiadis, P., Ruggieri, P., Müller, W. A., and Baehr, J: Hidden potential in predicting wintertime temperature anomalies in the Northern Hemisphere. Geophysical Research Letters, 49, e2021GL095063, https://doi.org/10.1029/2021GL095063, 2022.

Doms, G., and Schättler, U.: The nonhydrostatic limited-area model LM (Lokal-Modell) of DWD. Part I: Scientific documentation. Deutscher Wetterdienst Rep. LM F90 1.35, 172 pp. [Available from Deutscher Wetterdienst, P.O. Box 100465, 63004 Offenbach, Germany], 2004.

https://doi.org/10.5194/egusphere-2025-2473
Preprint. Discussion started: 12 June 2025

Donohue, K. A., Tracey, K. L., Watts, D. R., Chidichimo, M. P., and Chereskin, T. K.: Mean Antarctic Circumpolar Current transport measured in Drake Passage, Geophys. Res. Lett., 43, 11760–11767, https://doi.org/10.1002/2016GL070319, 2016.

Düsterhus, A., and Brune, S: The effect of initialisation on 20 year multi-decadal climate predictions. Clim Dyn 62, 831–840, https://doi.org/10.1007/s00382-023-06941-1, 2024.

Dunne, J. P., Hewitt, H. T., Arblaster, J., Bonou, F., Boucher, O., Cavazos, T., Durack, P. J., Hassler, B., Juckes, M., Miyakawa, T., Mizielinski, M., Naik, V., Nicholls, Z., O'Rourke, E., Pincus, R., Sanderson, B. M., Simpson, I. R., and Taylor, K. E.: An evolving Coupled Model Intercomparison Project phase 7 (CMIP7) and Fast Track in support of future climate assessment, EGUsphere, https://doi.org/10.5194/egusphere-2024-3874, 2024.

Elizalde, A., Romero-Mujalli, G., Stacke, T., and Hagemann, S.: Modeling Total Phosphorus Transport in the European Riverine System: Parameterization and Projections under Climate and Socioeconomic Scenarios, EGUsphere, https://doi.org/10.5194/egusphere-2024-3645, 2025.

Eyring, V., Bony, S., Meehl, G. A., Senior, C. A., Stevens, B., Stouffer, R. J., and Taylor, K. E.: Overview of the Coupled Model Intercomparison Project Phase 6 (CMIP6) experimental design and organization. Geoscientific Model Development., 9, 1937–1958, https://doi.org/10.5194/gmd-9-1937-2016, 2016.

Fieg, K., Gerdes, R., Fahrbach, E., Beszczynska-Möller, A., and Schauer, U.: Simulation of oceanic volume transports through Fram Strait 1995–2005, Ocean Dynam., 60, 491–502, https://doi.org/10.1007/s10236-010-0263-9, 2010.

Forster, P., T. Storelvmo, K. Armour, W. Collins, J.-L. Dufresne, D. Frame, D.J. Lunt, T. Mauritsen, M.D. Palmer, M. Watanabe, M. Wild, and H. Zhang, 2021: The Earth's Energy Budget, Climate Feedbacks, and Climate Sensitivity. In *Climate Change 2021: The Physical Science Basis. Contribution of Working Group I to the Sixth Assessment Report of the Intergovernmental Panel on Climate Change* [Masson-Delmotte, V., P. Zhai, A. Pirani, S.L. Connors, C. Péan, S. Berger, N. Caud, Y. Chen, L. Goldfarb, M.I. Gomis, M. Huang, K. Leitzell, E. Lonnoy, J.B.R. Matthews, T.K. Maycock, T. Waterfield, O. Yelekçi, R. Yu, and B. Zhou (eds.)]. Cambridge University Press, Cambridge, United Kingdom and New York, NY, USA, pp. 923–1054, doi: 10.1017/9781009157896.009.

https://doi.org/10.5194/egusphere-2025-2473
Preprint. Discussion started: 12 June 2025

Frajka-Williams, E., Ansorge ,I.J., Baehr, J., Bryden, H.L., Chidichimo, M.P., Cunningham, S.A., Danabasoglu, G., Dong, S., Donohue, K.A., Elipot, S., Heimbach, P., Holliday, N.P., Hummels, R., Jackson, L.C., Karstensen, J., Lankhorst, M., Le Bras, I.A., Lozier, M.S., McDonagh, E.L., Meinen, C.S., Mercier, H., Moat, B.I., Perez, R.C., Piecuch, C.G., Rhein, M., Srokosz, M.A., Trenberth, K.E., Bacon, S., Forget, G., Goni, G., Kieke, D., Koelling, J., Lamont, T., McCarthy, G.D., Mertens, C., Send, U., Smeed, D.A., Speich, S., van den Berg, M., Volkov, D. and Wilson, C.: Atlantic Meridional Overturning Circulation: Observed Transport and Variability. Front. Mar. Sci. 6:260. doi: 10.3389/fmars.2019.00260, 2019.

Fröhlich K., Dobrynin, M., Isensee, K., Gessner, C., Paxian, A., Pohlmann, H., Haak, H.,Brune, S., Früh, B., and Baehr, J.: The German Climate Forecast System: GCFS. J. Advances in Modeling Earth Systems, 13, https://doi.org/10.1029/2020MS002101, 2020.

Gelaro, R., McCarty, W., Suárez, M. J., Todling, R., Molod, A., Takacs, L., Randles, C. A., Darmenov, A., Bosilovich, M. G., Reichle, R., Wargan, K., Coy, L., Cullather, R., Draper, C., Akella, S., Buchard, V., Conaty, A., da Silva, A. M., Gu, W., Kim, G.-K., Koster, R., Lucchesi, R., Merkova, D., Nielsen, J. E., Partyka, G., Pawson, S., Putman, W., Rienecker, M., Schubert, S. D., Sienkiewicz, M., and Zhao, B.: The Modern-Era Retrospective Analysis for Research and Applications, Version 2 (MERRA-2), J. Climate, 30, 5419–5454, https://doi.org/10.1175/jcli-d-16-0758.1, 2017.

Giorgetta, M. A., Brokopf, R., Crueger, T., Esch, M., Fiedler, S., Helmert, J., Hohenegger, C., Kornblueh, L., Köhler, M., Manzini, E., Mauritsen, T., Nam, C., Raddatz, T., Rast, S., Reinert, D., Sakradzija, M., Schmidt, H., Schneck, R., Schnur, R., Silvers, L., Wan. H., Zängl, G., and Stevens, B. : ICON-A, the Atmosphere Component of the ICON Earth System model: I. Model Description, Journal of Advances in Modeling Earth Systems, vol. 10, no. 7, pp. 1613–1637, doi:10.1029/2017MS001242, 2018.

Giorgetta, M. A., Manzini, E., and Roeckner, E.: Forcing of the quasi-biennial oscillation from a broad spectrum of atmospheric waves, Geophysical Research Letters, vol. 29, no. 8, Art. no. 1245, doi:10.1029/2002GL014756, 2002.

Gordon, A. L., Sprinthall, J., Van Aken, H. M., Susanto, D., Wijffels, S., Molcard, R., Field, A., Pranowo, W., and Wirasantosa, S.: The Indonesian throughflow during 2004–2006 as observed by the INSTANT program, Dyn. Atmos. Oceans, 50, 115–128, https://doi.org/10.1016/j.dynatmoce.2009.12.002, 2010.

https://doi.org/10.5194/egusphere-2025-2473
Preprint. Discussion started: 12 June 2025

Gray, L. J., Anstey, J. A., Kawatani, Y., Lu, H., Osprey, S., and Schenzinger, V.: Surface impacts of the Quasi Biennial Oscillation, Atmos. Chem. Phys., 18, 8227–8247, https://doi.org/10.5194/acp-18-8227-2018, 2018.

Gregory, J. M.: A new method for diagnosing radiative forcing and climate sensitivity, Geophysical Research Letters, vol. 31, no. 3, Art. no. L03205, doi:10.1029/2003GL018747, 2004.

Guilyardi, E., Capotondi, A., Lengaigne, M., Thual, S. and Wittenberg, A.T.: ENSO Modeling. In El Niño Southern Oscillation in a Changing Climate (eds M.J. McPhaden, A. Santoso and W. Cai), https://doi.org/10.1002/9781119548164.ch9, 2020.

Gulev, S.K., Thorne, P. W., Ahn, J., Dentener, F. J., Domingues, C. M., Gerland, S, Gong, D., Kaufman, D. S., Nnamchi, H. C., Quaas, J., Rivera, J. A., Sathyendranath, S., Smith, S. L., Trewin, B., von Schuckmann, K., and Vose, R. S.: Changing State of the Climate System. In Climate Change 2021: The Physical Science Basis. Contribution of Working Group I to the Sixth Assessment Report of the Intergovernmental Panel on Climate Change, 2021.

[Masson-Delmotte, V., P. Zhai, A. Pirani, S.L. Connors, C. Péan, S. Berger, N. Caud, Y. Chen, L. Goldfarb, M.I. Gomis, M. Huang, K. Leitzell, E. Lonnoy, J.B.R. Matthews, T.K. Maycock, T. Waterfield, O. Yelekçi, R. Yu, and B. Zhou (eds.)]. Cambridge University Press, Cambridge, United Kingdom and New York, NY, USA, pp. 287–422, doi: 10.1017/9781009157896.004.

Gutjahr, O., Putrasahan, D., Lohmann, K., Jungclaus, J. H., von Storch, J.-S., Brüggemann, N., Haak, H., and Stössel, A.: Max Planck Institute Earth System model (MPI-ESM1.2) for the High-Resolution Model Intercomparison Project (HighResMIP), Geosci. Model Dev., 12, 3241–3281, https://doi.org/10.5194/gmd-12-3241-2019, 2019.

Hagemann, S., Ho-Hagemann, H.T.M., and Hanke, M.: The Hydrological Discharge Model - a river runoff component for offline and coupled model applications (5.2.3). Zenodo, https://doi.org/10.5281/zenodo.14179917, 2023.

Hagemann, S., Stacke, T., and Ho-Hagemann, H.T.M.: High resolution discharge simulations over Europe and the Baltic Sea catchment. Front. Earth Sci., 8:12. doi: 10.3389/feart.2020.00012, 2020.

https://doi.org/10.5194/egusphere-2025-2473
Preprint. Discussion started: 12 June 2025

Hajima, T., Kawamiya, M., Ito, A., Tachiiri, K., Jones, C., Arora, V., Brovkin, V., Séférian, R., Liddicoat, S., Friedlingstein, P., and Shevliakova, E.: Consistency of global carbon budget between concentration- and emission-driven historical experiments simulated by CMIP6 Earth system models and suggestion for improved simulation of CO_2 concentration, EGUsphere, https://doi.org/10.5194/egusphere-2024-188, 2024.

Hanke, M., Redler, R., Holfeld, T., and Yastremsky, M.: YAC 1.2.0: new aspects for coupling software in Earth system modelling, *Geoscientific Model Development*, 9(8), 2755–2769, 2016.

Hansen, B., Østerhus, S., Turrell, W. R., Jónsson, S., Valdimarsson, H., Hátún, H., and Olsen, S. M.: The Inflow of Atlantic Water, Heat, and Salt to the Nordic Seas Across the Greenland–Scotland Ridge, pp. 15–43, Springer Netherlands, Dordrecht, https://doi.org/10.1007/978-1-4020-6774-7_2, 2008.

Heidinger, A. K., M. J. Foster, A. Walther, and X. Zhao: The Pathfinder Atmospheres–Extended AVHRR Climate Dataset. Bull. Amer. Meteor. Soc., 95, 909–922, https://doi.org/10.1175/BAMS-D-12-00246.1, 2014.

Hersbach, H., Bell, B., Berrisford, P., Hirahara, S., Horányi, A., Muñoz-Sabater, J., Nicolas, J., Peubey, C., Radu, R., Schepers, D., Simmons, A., Soci, C., Abdalla, S., Abellan, X., Balsamo, G., Bechtold, P., Biavati, G., Bidlot, J., Bonavita, M., De Chiara, G., Dahlgren, P., Dee, D., Diamantakis, M., Dragani, R., Flemming, J., Forbes, R., Fuentes, M., Geer, A., Haimberger, L., Healy, S., Hogan, R. J., Hólm, E., Janisková, M., Keeley, S., Laloyaux, P., Lopez, P., Lupu, C., Radnoti, G., de Rosnay, P., Rozum, I., Vamborg, F., Villaume, S., and Thépaut, J.-N.: The ERA5 global reanalysis, Quarterly Journal of the Royal Meteorological Society, 146, 1999–2049, https://doi.org/https://doi.org/10.1002/qj.3803, 2020.

Hettrich, S., Müller, W. A., Cubasch, U., Feldmann, H., Früh, B., Grieger, J, Kadow, C, Kaspar, F, Kottmeier, C., Paxian, A., Polkova, I,. Scheffler, J., Stammer, D., Tiedje, B., Ulbrich, U., Vamborg, F. S. E., and Marotzke, J.: MiKlip – turning a scientific concept into a pre-operational system for decadal climate predictions, PROMET, 104(6), https://doi.org/10.5676/dwd_pub/promet_104_06, 2021.

Hogan, R. J., and Bozzo, A.: A flexible and efficient radiation scheme for the ECMWF model. Journal of Advances in Modeling Earth Systems, 10, 1990–2008, https://doi.org/10.1029/2018MS001364, 2018.

https://doi.org/10.5194/egusphere-2025-2473
Preprint. Discussion started: 12 June 2025

Hohenegger, C., Korn, P., Linardakis, L., Redler, R., Schnur, R., Adamidis, P., Bao, J., Bastin, S., Behravesh, M., Bergemann, M., Biercamp, J., Bockelmann, H., Brokopf, R., Brüggemann, N., Casaroli, L., Chegini, F., Datseris, G., Esch, M., George, G., Giorgetta, M., Gutjahr, O., Haak, H., Hanke, M., Ilyina, T., Jahns, T., Jungclaus, J., Kern, M., Klocke, D., Kluft, L., Kölling, T., Kornblueh, L., Kosukhin, S., Kroll, C., Lee, J., Mauritsen, T., Mehlmann, C., Mieslinger, T., Naumann, A. K., Paccini, L., Peinado, A., Praturi, D. S., Putrasahan, D., Rast, S., Riddick, T., Roeber, N., Schmidt, H., Schulzweida, U., Schütte, F., Segura, H., Shevchenko, R., Singh, V., Specht, M., Stephan, C. C., von Storch, J.-S., Vogel, R., Wengel, C., Winkler, M., Ziemen, F., Marotzke, J., and Stevens, B.: ICON-Sapphire: simulating the components of the Earth system and their interactions at kilometer and subkilometer scales, Geosci. Model Dev., 16, 779–811, https://doi.org/10.5194/gmd-16-779-2023, 2023.

Holton, J. R. and Tan, H.-C.: The Quasi-Biennial Oscillation in the Northern Hemisphere Lower Stratosphere", Journal of the Meteorological Society of Japan, vol. 60, no. 1, pp. 140–148, 1982. doi:10.2151/jmsj1965.60.1_140.

Hoskins, B. J., James, I. N., and White, G. H.: The shape, propagation and mean-flow interaction of large-scale weather systems. Journal of Atmospheric Sciences, 40, 1595–1612, 1983.

Ilyina, T., Six, K. D., Segschneider, J., Maier-Reimer, E., Li, H., & Núñez-Riboni, I.: Global ocean biogeochemistry model HAMOCC: Model architecture and performance as component of the MPI-Earth system model in different CMIP5 experimental realizations. Journal of Advances in Modeling Earth Systems, 5(2), 287–315. https://doi.org/10.1029/2012ms000178, 2013.

IPCC, 2023: Sections. In: Climate Change: Synthesis Report. Contribution of Working Groups I, II and III to the Sixth Assessment Report of the Intergovernmental Panel on Climate Change [Core Writing Team, H. Lee and J. Romero (eds.)]. IPCC, Geneva, Switzerland, pp. 35-115, doi: 10.59327/IPCC/AR6-9789291691647, 2023.

Jochumsen, K., Quadfasel, D., Valdimarsson, H., and Jónsson, S.: Variability of the Denmark Strait overflow: Moored time series from 1996–2011, J. Geophys. Res. 117, C12003, https://doi.org/10.1029/2012JC008244, 2012.

https://doi.org/10.5194/egusphere-2025-2473
Preprint. Discussion started: 12 June 2025

Jungclaus, J. H., Lorenz, S. J., Schmidt, H., Brovkin, V., Brüggemann, N., Chegini, F., Crüger, T., De-Vrese, P., Gayler, V., Giorgetta, M. A., Gutjahr, O., Haak, H., Hagemann, S., Hanke, M., Ilyina, T., Korn, P., Kröger, J., Linardakis, L., Mehlmann, C., Mikolajewicz, U., Müller, W.A., Nabel, J. E. M. S., Notz, D., Pohlmann, H., Putrasahan, D., A., Raddatz, T., Ramme, L., Redler, R., Reick, C. H., Riddick, T., Sam, T., Schneck, R., Schnur, R., Schupfner, M., von Storch, J.-S., Wachsmann, F., Wieners, K.-H., Ziemen, F., Stevens, B., Marotzke, J., Claussen, M. "The ICON Earth System Model Version 1.0", Journal of Advances in Modeling Earth Systems, vol. 14, no. 4, Art. no. e2021MS002813, doi:10.1029/2021MS00281310.1002/essoar.10507989.1, 2022.

Korn, P.: Formulation of an unstructured grid model for global ocean dynamics. *Journal of Computational Physics*, **339**, 525– 552, https://doi.org/10.1016/j.jcp.2017.03.009, 2017.

Korn, P., Brüggemann, N.; Jungclaus, J. H.; Lorenz, S. J.; Gutjahr,O.; Haak, H.; Linardakis, L.; Mehlmann, C.; Mikolajewicz, U.; Notz, D.;Putrasahan, D. A.; Singh, V.; von Storch, J. - S.; Zhu, X.; Marotzke, J.: ICON-O: The Ocean Component of the ICON Earth System Model—Global Simulation Characteristics and Local Telescoping Capability, Journal of Advances in Modeling Earth Systems, vol. 14, no. 10, Art. no. e2021MS002952, doi:10.1029/2021MS002952, 2022.

Kruschke, T., Rust, H. W., Kadow, C., Müller, W. A., Pohlmann, H., Leckebusch, G. C., and Ulbrich, U.: Probabilistic evaluation of decadal prediction skill regarding Northern Hemisphere winter storms. Met. Zeitschrift, 25, 721-738 doi:10.1127/metz/2015/0641, 2016.

Kushnir Y., Scaife, A.A., Arritt, R. et al.: Towards Operational Predictions of the Near-Term Climate. Nature Climate Change, 9, 94–101, https://doi.org/10.1038/s41558-018-0359-7, 2019.

Leuenberger, D., Koller, M., Fuhrer, O., and Schär, C.: A Generalization of the SLEVE Vertical Coordinate, Monthly Weather Review, vol. 138, no. 9, AMS, pp. 3683–3689, doi:10.1175/2010MWR3307.1, 2010.

l'Heureux M., Tippett, M. K., and Wang, W.: Prediction challenges from errors in tropical Pacific sea surface temperature trends. Frontiers in Climate, 4. doi:103389/fclim.2022.837483, 2022.

Li, H., Ilyina, T., Müller, W. A., and Sienz, F.: Decadal predictions of the North Atlantic CO_2 uptake. Nat Commun., 11076, https://doi.org/10.1038/ncomms11076, 2016.

https://doi.org/10.5194/egusphere-2025-2473
Preprint. Discussion started: 12 June 2025

Li, H., Ilyina, T., Loughran, T., Spring, A., and Pongratz, J.: Reconstructions and predictions of the global carbon budget with an emission-driven Earth system model, Earth Syst. Dynam., 14, 101–119, 2023.

Liao, H., Cai, Z., Guo, J., and Song, Z.: Effects of ITCZ Poleward Location Bias on ENSO Seasonal Phase-Locking Simulation in Climate Models. Journal of Climate, 36(15), 5233-5249. https://doi.org/10.1175/JCLI-D-22-0891.1, 2023.

Luo, F., Ying, J., Liu, T. and Chen, D.: Origins of Southern Ocean warm sea surface temperature bias in CMIP6 models, npj Climate and Atmospheric Science 6:127, https://doi.org/10.1038/s41612-023-00456-6, 2023.

Loeb, N. G., Doelling, D. R., Wang, H., Su, W., Nguyen, C., Corbett, J. G., Liang, L., Mitrescu, C., Rose, F. G., and Kato, S.: Clouds and the Earth’s Radiant Energy System (CERES) Energy Balanced and Filled (EBAF) Top-of-Atmosphere (TOA) Edition-4.0 Data Product, Journal of Climate, 31, 895–918, https://doi.org/10.1175/jcli-d-17-0208.1, 2018.

Maerz, J., Six, K. D., Stemmler, I., Ahmerkamp, S., and Ilyina, T.: Microstructure and composition of marine aggregates as co-determinants for vertical particulate organic carbon transfer in the global ocean. Biogeosciences, 17(7), 1765–1803, https://doi.org/10.5194/bg-17-1765-2020, 2020.

Maher, N., Milinski, S., Suarez-Gutierrez, L., Botzet, M., Dobrynin, M., Kornblueh, L., et al.: The Max Planck Institute Grand Ensemble: Enabling the exploration of climate system variability. Journal of Advances in Modeling Earth Systems, 11, 2050–2069. https://doi.org/10.1029/2019MS001639, 2019.

Manzini, E., et al.: Northern winter climate change: Assessment of uncertainty in CMIP5 projections related to stratosphere-troposphere coupling, *J. Geophys. Res. Atmos.*, 119, 7979–7998, doi:10.1002/2013JD021403, 2014.

Marotzke, J., Müller, W. A., Vamborg, F. S. E., Becker, P., Cubasch, U., Feldmann, H., Kaspar, F., Kottmeier, C., Marini, C., Polkova, I., Prömmel, K., Rust, H. W., Stammer, D., Ulbrich, U., Kadow, C., Köhl, A., Kröger, J., Kruschke, T., Pinto, J. G., Pohlmann, H., Reyers, M., Schröder, M., Sienz, F., Timmreck, C., and Ziese, M.: MiKlip - A National Research Project on Decadal Climate Prediction. Bull. Amer. Meteor. Soc., 97, 2379–2394, https://doi.org/10.1175/BAMS-D-15-00184.1, 2016.

https://doi.org/10.5194/egusphere-2025-2473
Preprint. Discussion started: 12 June 2025

Martin, Z., Son, S.-W., Butler, A., Hendon, H., Kim, H., Sobel, A., Yoden, S., and Zhang, C., The influence of the quasi-biennial oscillation on the Madden-Julian oscillation, Nature Reviews Earth and Environment, 2, 477-489, doi: 10.1038/s43017-021-00173-9, 2021.

M. Mathis, Logemann, K., Maerz, J., Lacroix, F., Hagemann, S., Chegini, F., Ramme, L., Ilyina, T., Korn, P., and Schrum, C.: Seamless integration of the coastal ocean in global marine carbon cycle modeling, 14,8, doi: 10.1029/2021MS002789, 2022.

Mauritsen, T., Bader, J., Becker, T., Behrens, J., Bittner, M., Brokopf, R., Brovkin, V., Claussen, M., Crueger, T., Esch, M., Fast, I., Fiedler, S., Fläschner, D., Gayler, V., Giorgetta, M., Goll, D. S., Haak, H., Hagemann, S., Hedemann, C., Hohenegger, C., Ilyina, T., Jahns, T., Jimenéz-de-la-Cuesta, D., Jungclaus, J., Kleinen, T., Kloster, S., Kracher, D., Kinne, S., Kleberg, D., Lasslop, G., Kornblueh, L., Marotzke, J., Matei, D., Meraner, K., Mikolajewicz, U., Modali, K., Möbis, B., Müller, W. A., Nabel, J. E. M. S., Nam, C. C. W., Notz, D., Nyawira, S.-S., Paulsen, H., Peters, K., Pincus, R., Pohlmann, H., Pongratz, J., Popp, M., Raddatz, T. J., Rast, S., Redler, R., Reick, C. H., Rohrschneider, T., Schemann, V., Schmidt, H., Schnur, R., Schulzweida, U., Six, K. D., Stein, L., Stemmler, I., Stevens, B., von Storch, J.-S., Tian, F., Voigt, A., Vrese, P., Wieners, K.-H., Wilkenskjeld, S., Winkler, A., and Roeckner, E.: Developments in the MPI-M Earth System Model version 1.2 (MPI-ESM1.2) and its response to increasing CO_2, J. Adv. Model. Earth Sy., 11, 998–1038, https://doi.org/10.1029/2018MS001400, 2018.

Mehlmann, C., and Korn, P.: Sea-ice dynamics on triangular grids. *Journal of Computational Physics*, 428, 110086., 2021.

Mehlmann C., Danilov, S., Losch, M., Lemiuex, J. F., Hutterer, N., Richter, T., Plain, P., Hunke, E. C., and Korn, P.: Simulating Linear Kinematic Features in Viscous-Plastic Sea Ice Models on Quadrilateral and Triangular Grids With Different Variable Staggering, Journal of Advances in Modeling Earth Systems, 10.1029/2021MS002523, 2012.

Morice, C. P., Kennedy, J. J., Rayner, N. A., Winn, J. P., Hogan, E., Killick, R. E., Dunn, R. J. H., Osborn, T. J., Jones, P. D., and Simpson, I. R.: An Updated Assessment of Near-Surface Temperature Change From 1850: The HadCRUT5 Data Set, Journal of Geophysical Research: Atmospheres, 126, https://doi.org/10.1029/2019jd032361, 2021.

https://doi.org/10.5194/egusphere-2025-2473
Preprint. Discussion started: 12 June 2025

Müller, W. A., Appenzeller, C. and Schär, C.: Probabilistic seasonal prediction of the winter North Atlantic Oscillation and its impact on near surface temperature, Clim. Dyn., 24, 213-226, 2005.

Müller, W. A., Baehr, J., Haak, H., Jungclaus, J. H, Kröger, J., Matei, D., Notz, D., Pohlmann, H, von Storch J.-S., and Marotzke, J.: Forecast skill of multi-year seasonal means in the decadal prediction system of the Max Planck Institute for Meteorology. Geophys. Res. Lett., 39, L22707. doi:10.1029/2012GL053326, 2012.

Müller, W. A., Jungclaus, J. H., Mauritsen, T., Baehr, J., Bittner, M., Budich, R., Bunzel, F., Esch, M., Ghosh, R., Haak, H., Ilyina, T., Kleine, T., Kornblueh, L., Li, H., Modali, K., Notz, D., Pohlmann, H., Roeckner, E., Stemmler, I., Tian, F., and Marotzke, J.: A higher-resolution version of the Max Planck Institute Earth System Model (MPI-ESM 1.2-HR), J. Adv. Model. Earth Sy., 10, 1383–1413, https://doi.org/10.1029/2017MS001217, 2018.

Müller, W. A., B. Früh, P. Korn, R. Potthast, J. Baehr, J.-M. Bettems, G. Bölöni, S. Brienen, K. Fröhlich, J. Helmert, J. Jungclaus, M. Köhler, S. Lorenz, A. Schneidereit, R. Schnur, J.-P. Schulz, L. Schlemmer, C. Sgoff, T. V. Pham, H. Pohlmann, B. Vogel, H. Vogel, R. Wirth, S. Zaehle, G. Zängl, B. Stevens, and J. Marotzke: ICON: Towards vertically integrated model configurations for numerical weather prediction, climate predictions and projections, Bull. Am. Met. Soc, https://doi.org/10.1175/BAMS-D-24-0042.1, 2025.

Müller, W. A., Lorenz, S., Pham, T. V., Schneidereit, A., Brokopf, R., Brovkin, V., Brüggemann, N., Castro-Morales, K., Chegini, F., Dommenget, D., Engels, F., Fröhlich, K., Früh, B., Gayler, V., Haak, H., Hagemann, S., Hanke, M., Ilyina, T., Jungclaus, J., Köhler, M., Korn, P., Kornblueh, L., Kroll, C., Krüger, J., Nabel, J., Niemeier, U., Potthast, R., Riddick, T., Pohlmann, H., Polkova, I., Riddick, T., Schlund, M., Schnur, R., S., C., Stacke, T., Wirth, R., Yu, D., Zaehle, S., Marotzke, J.: "Source code and scripts for publication "The ICON-based coupled Earth System Model for Climate Predictions and Projections (ICON XPP)"", https://doi.org/10.17617/3.UUIIZ8, Edmond, V3, 2024.

Nabel, J. E. M., Naudts, S. K., and Pongratz, J.: Accounting for forest age in the tile-based dynamic global vegetation model JSBACH4 – a land surface model for the ICON-ESM. *Geoscientific Model Development*, **13**, 185–200, https://doi.org/10.5194/gmd-13-185-2020, 2020.

https://doi.org/10.5194/egusphere-2025-2473
Preprint. Discussion started: 12 June 2025

Nielsen, D.M., Chegini, F., Maerz, J. et al. Reduced Arctic Ocean CO_2 uptake due to coastal permafrost erosion. Nat. Clim. Chang. 14, 968–975, https://doi.org/10.1038/s41558-024-02074-3, 2024.

Niemeier, U., Wallis, S., Timmreck, C., van Pham, T., & von Savigny, C.: How the Hunga Tonga—Hunga Ha'apai water vapor cloud impacts its transport through the stratosphere: Dynamical and radiative effects. *Geophysical Research Letters*, 50, e2023GL106482. https://doi.org/10.1029/2023GL106482, 2023.

Nowlin Jr., W. D. and Klinck, J. M.: The physics of the Antarctic Circumpolar Current, Rev. Geophys., 24, 469–491, https://doi.org/10.1029/RG024i003p00469, 1986.

Olsen, A., Key, R. M., Van Heuven, S., Lauvset, S. K., Velo, A., Lin, X., et al.: The Global Ocean Data Analysis Project version 2 (GLODAPv2)–an internally consistent data product for the world ocean. Earth System Science Data, 8(2), 297–323. https://doi.org/10.5194/essd-8-297-2016, 2016.

Paulsen, H., Ilyina, T., Six, K. D., & Stemmler, I.:. Incorporating a prognostic representation of marine nitrogen fixers into the global ocean biogeochemical model HAMOCC. Journal of Advances in Modeling Earth Systems, 9(1), 438–464. https://doi.org/10.1002/2016ms000737, 2017.

Planton, Y. Y., Guilyardi, E., Wittenberg, A. T., Lee, J., Gleckler, P. J., Bayr, T., McGregor, S., McPhaden, M. J., Power, S., Roehrig, R., Voldoire, A.:Evaluating Climate Models with the CLIVAR 2020 ENSO Metrics Package. Bull. Amer. Meteor. Soc., 102, E193–E217, https://doi.org/10.1175/BAMS-D-19-0337.1, 2021.

Platnick, S., King, M., Ackerman, S., Menzel, W., Baum, B., Riedi, J., and Frey, R.: The MODIS cloud products: algorithms and examples from Terra, IEEE Transactions on Geoscience and Remote Sensing, 41, 459–473, https://doi.org/10.1109/TGRS.2002.808301, 2003.

Pohlmann, H., W. A. Müller, K. Kulkarni, M. Kameswarrao, D. Matei, F. S. E. Vamborg, C. Kadow, S. Illing, J. Marotzke: Improved forecast skill in the tropics in the new MiKlip decadal climate predictions. Geophys. Res. Lett., 40, 5798-5802. doi:10.1002/2013GL058051, 2013.

https://doi.org/10.5194/egusphere-2025-2473
Preprint. Discussion started: 12 June 2025

Praveen Kumar, B., Vialard J., Lengaigne, M., Murty, V. S. N. , and McPhaden, M. J.: TropFlux: Air-Sea Fluxes for the Global Tropical Oceans - Description and evaluation, Climate Dynamics, 38, 1521-1543, doi:10.1007/s00382-011-1115-0, 2012.

Priestley, M. D. K., Ackerley, D., Catto, J. L., Hodges, K. I., McDonald, R. E., and Lee, R. W.: An Overview of the Extratropical Storm Tracks in CMIP6 Historical Simulations. *J. Climate*, **33**, 6315–6343, https://doi.org/10.1175/JCLI-D-19-0928.1, 2020.

Priestley, M. D. K., Ackerley, D., Catto, J, L., and Hodge, K. I.: Drivers of Biases in the CMIP6 Extratropical Storm Tracks. Part I: Northern Hemisphere. *J. Climate*, **36**, 1451–1467, https://doi.org/10.1175/JCLI-D-20-0976.1, 2023.

Prill, F., Reinert, D., Rieger, D., and Zängl, G.: ICON Tutorial -Working with the ICON model. Technical report, Deutscher Wetterdienst, https://doi.org/10.5676/DWD_pub/nwv/icon_tutorial2024, 2023.

Riddick, T.: Generation of HD parameters files for ICON grids: Technical note, Berichte zur Erdsystemforschung, 245, https://doi.org/10.17617/2.3336390, 2021.

Riddick, T., Brovkin, V., Hagemann, S., and Mikolajewicz, U.: Dynamic hydrological discharge modelling for coupled climate model simulations of the last glacial cycle: the MPI-DynamicHD model version 3.0, Geosci. Model Dev., 11, 4291–4316, https://doi.org/10.5194/gmd-11-4291-2018, 2018.

Reick, C. H., Raddatz, T., Brovkin, V., and Gayler, V.: Representation of natural and anthropogenic land cover change in MPI-ESM. *J. Advances in Modeling Earth Systems*, **5**, 459–482, https://doi.org/10.1002/jame.20022, 2013.

Reick, C. H., Gayler, V., Goll, D., Hagemann, S., Heidkamp, M., and Nabel, J. E. M. S.: JSBACH 3 - The land component of the MPI Earth System Model: Documentation of version 3.2. Berichte zur Erdsystemforschung, 240, 2021.

Righi, M., Andela, B., Eyring, V., Lauer, A., Predoi, V., Schlund, M., Vegas-Regidor, J., Bock, L., Brötz, B., de Mora, L., Diblen, F., Dreyer, L., Drost, N., Earnshaw, P., Hassler, B., Koldunov, N., Little, B., Loosveldt Tomas, S., and Zimmermann, K.: Earth System Model Evaluation Tool (ESMValTool) v2.0 – technical overview, Geoscientific Model Development, 13, 1179–1199, https://doi.org/10.5194/gmd-13-1179-2020, 2020.

https://doi.org/10.5194/egusphere-2025-2473
Preprint. Discussion started: 12 June 2025

Rossby, T. and Flagg, C.: Direct measurement of volume flux in the Faroe-Shetland Channel and over the Iceland-Faroe Ridge, Geophys. Res. Lett., 39, L07602, https://doi.org/10.1029/2012GL051269, 2012.

Scaife, A.A., Arribas, A., Blockley, E., Brookshaw, A., Clark, R. T., Dunstone, N., et al.: Skillful long-range prediction of European and North American winters. Geophys. Res. Lett. 41, 2514–2519, https://doi.org/10.1002/2014GL059637, 2014.

Scaife, A. A., et al., "Long-range prediction and the stratosphere", Atmospheric Chemistry & Physics, vol. 22, no. 4, pp. 2601–2623, 2022. doi:10.5194/acp-22-2601-2022.

Schlund, M., Hassler, B., Lauer, A., Andela, B., Jöckel, P., Kazeroni, R., Tomas, S. L., Medeiros, B., Predoi, V., Sénési, S., Servonnat, J., Stacke, T., Vegas-Regidor, J., Zimmermann, K., and Eyring, V.: Evaluation of native Earth system model output with ESMValTool v2.6.0, Geoscientific Model Development, 16, 315–333, https://doi.org/10.5194/gmd-16-315-2023, 2023.

Schneck, R., Gayler, V., Nabel, J. E. M. S., Raddatz, T., Reick, C. H., and Schnur, R.: Assessment of JSBACHv4.30 as a land component of ICON-ESM-V1 in comparison to its predecessor JSBACHv3.2 of MPI-ESM1.2. *Geoscientific Model Development*, **15**, https://doi.org/10.5194/gmd-15-8581-2022, 2022.

Schröder, M., Danne, O., Falk, U., Niedorf, A., Preusker, R., Trent, T., Brockmann, C., Fischer, J., Hegglin, M., Hollmann, R., Pinnock, S.: A combined high resolution global TCWV product from microwave and near infrared imagers - COMBI, Satellite Application Facility on Climate Monitoring, https://doi.org/10.5676/EUM_SAF_CM/COMBI/V001, 2023.

Schulz, J.-P., Dümenil, L., Polcher, J., Schlosser, C. A., and Xue, Y.: Land surface energy and moisture fluxes: Comparing three models, *J. Appl. Meteor.*, **37**, 288–307, https://doi.org/10.1175/1520-0450(1998)037<0288:LSEAMF>2.0.CO;2, 1998.

Schuster , M., Grieger, J., Richling, A., Schartner, T., Illing, S., Kadow, C., Müller, W. A., Pohlmann, H., Pfahl, S., and Ulbrich, U.: Improvement in the decadal prediction skill of the northern hemisphere extra-tropical winter circulation through increased model resolution. Earth System Dynamics, 10, 901-917, doi:10.5194/esd-2019-18, 2019.

Schweiger, A., Lindsay, R., Zhang, J., Steele, M., and Stern, H.: Uncertainty in modeled arctic sea ice volume, J. Geophys. Res., doi:10.1029/2011JC007084, 2011.

https://doi.org/10.5194/egusphere-2025-2473
Preprint. Discussion started: 12 June 2025

Semtner,A.J.:A model for the thermodynamic growth of sea ice in numerical investigations of climate J.Phys.Oceanogr.6, 379-389, 1976.

Smith, D.M., Eade, R., Scaife, A., Caron, L.-P., Danabasoglu, G., DelSole, T., et al. .: Robust skill of decadal climate predictions. npj Cli*m Atmos Sci* **2**, 13, https://doi.org/10.1038/s41612-019-0071-y, 2019.

Smith, D.M., Scaife, A. A., Eade, R., Athanasiadis, P., Bellucci, A., Bethke, I., et al.: North Atlantic climate far more predictable than models imply, Nature, 583, 796-800, htpps://doi:10.1038/s41586-020-2525-0, 2020.

Smith, D., Eade, R., Andrews, M. B., Ayres, H., Clark, A., Chripko, S, Deser, C. Dunstone, N.J., García-Serrano, J., Gastineau, G., Graff, L. S., Hardiman, S.C., He, B., Hermanson, L., Jung, T., Knight, J., Levine, X., Magnusdottir, G., Manzini, E., Matei, D., Mori, M., Msadek, R., Ortega, P., Peings, Y., Scaife, A.A., Screen, J.A., Seabrook, M.,Semmler, T., Sigmond, M., Streffing, J., Sun, L., Walsh, A.: Robust but weak winter atmospheric circulation response to future Arctic sea ice loss. Nat. Commun., 13, 727, https://doi.org/10.1038/s41467-022-28283-y., 2022.

Steele, M., Morley, R., and Ermold, W.: PHC: A global ocean hydrography with a high-quality Arctic Ocean, J. Climate, 14, 2079-2087, 2001.

Stengel, M., Stapelberg, S., Sus, O., Finkensieper, S., Würzler, B., Philipp, D., Hollmann, R., Poulsen, C., Christensen, M., and McGarragh, G.: Cloud_cci Advanced Very High Resolution Radiometer post meridiem (AVHRR-PM) dataset version 3: 35-year climatology of global cloud and radiation properties, Earth Syst. Sci. Data, 12, 41–60, https://doi.org/10.5194/essd-12-41-2020, 2020.

Woodgate, R. A., Aagard, K., and Weingartner, T. J.: Interannual changes in the Bering Strait fluxes of volume, heat, and freshwater between 1991 and 2004, Geophys. Res. Lett., 33, L15609, https://doi.org/10.1029/2006GL026931, 2006.

Woodgate, R. A., Weingartner, T., and Lindsa, R.: Observed increases in Bering Strait oceanic fluxes from the Pacific to the Arctic from 2001 to 2011 and their impacts on the Arctic Ocean water column, Geophys. Res. Lett., 39, L24603, https://doi.org/10.1029/2012GL054092, 2012.

Zängl, G., Reinert, D., Rípodas, P., and Baldauf, M.: The ICON (ICOsahedral Non-hydrostatic) modelling framework of DWD and MPI-M: Description of the non-hydrostatic

https://doi.org/10.5194/egusphere-2025-2473
Preprint. Discussion started: 12 June 2025

dynamical core, Quarterly Journal of the Royal Meteorological Society, vol. 141, no. 687, pp. 563–579, doi:10.1002/qj.2378, 2015.

Zhang, J. L. and Rothrock, D. A.: Modeling global sea ice with a thickness and enthalpy distribution model in generalized curvilinear coordinates, Mon. Weather Rev., 131, 845-861, 2003.